J. Fluid Mech. (2008), *vol.* 612, *pp.* 201–236.
doi:10.1017/S0022112008003029 Printed in the United Kingdom

Bubble-induced skin-friction drag reduction and the abrupt transition to air-layer drag reduction

BRIAN R. ELBING, ERIC S. WINKEL, KEARY A. LAY, STEVEN L. CECCIO, DAVID R. DOWLING AND MARC PERLIN

Department of Mechanical Engineering University of Michigan, Ann Arbor, MI 48109, USA

(Received 14 February 2008 and in revised form 10 June 2008)

To investigate the phenomena of skin-friction drag reduction in a turbulent boundary layer (TBL) at large scales and high Reynolds numbers, a set of experiments has been conducted at the US Navy's William B. Morgan Large Cavitation Channel (LCC). Drag reduction was achieved by injecting gas (air) from a line source through the wall of a nearly zero-pressure-gradient TBL that formed on a flat-plate test model that was either hydraulically smooth or fully rough. Two distinct drag-reduction phenomena were investigated; bubble drag reduction (BDR) and air-layer drag reduction (ALDR).

The streamwise distribution of skin-friction drag reduction was monitored with six skin-friction balances at downstream-distance-based Reynolds numbers to 220 million and at test speeds to 20.0 m s^{-1}. Near-wall bulk void fraction was measured at twelve streamwise locations with impedance probes, and near-wall ($0 < Y < 5$ mm) bubble populations were estimated with a bubble imaging system. The instrument suite was used to investigate the scaling of BDR and the requirements necessary to achieve ALDR.

Results from the BDR experiments indicate that: significant drag reduction (>25 %) is limited to the first few metres downstream of injection; marginal improvement was possible with a porous-plate versus an open-slot injector design; BDR has negligible sensitivity to surface tension; bubble size is independent of surface tension downstream of injection; BDR is insensitive to boundary-layer thickness at the injection location; and no synergetic effect is observed with compound injection. Using these data, previous BDR scaling methods are investigated, but data collapse is observed only with the 'initial zone' scaling, which provides little information on downstream persistence of BDR.

ALDR was investigated with a series of experiments that included a slow increase in the volumetric flux of air injected at free-stream speeds to 15.3 m s^{-1}. These results indicated that there are three distinct regions associated with drag reduction with air injection: Region I, BDR; Region II, transition between BDR and ALDR; and Region III, ALDR. In addition, once ALDR was established: friction drag reduction in excess of 80 % was observed over the entire smooth model for speeds to 15.3 m s^{-1}; the critical volumetric flux of air required to achieve ALDR was observed to be approximately proportional to the square of the free-stream speed; slightly higher injection rates were required for ALDR if the surface tension was decreased; stable air layers were formed at free-stream speeds to 12.5 m s^{-1} with the surface fully roughened (though approximately 50 % greater volumetric air flux was required); and ALDR was sensitive to the inflow conditions. The sensitivity to the inflow conditions

can be mitigated by employing a small faired step (10 mm height in the experiment) that helps to create a fixed separation line.

1. Introduction

Skin-friction drag is an important component of resistance in nearly all transportation systems moving in a fluid. Thus, skin-friction reduction techniques have been investigated for several decades and these prior investigations have shown that skin-friction drag reduction can be achieved by injecting gas (air) into the near-wall region of a liquid (water) turbulent boundary layer (TBL). Bubble drag reduction (BDR), has been shown to produce local drag reduction in excess of 80 % in laboratory-scale experiments, and has therefore attracted the interest of numerous investigators. Unfortunately, the majority of BDR experiments to date have been conducted at low Reynolds numbers (to the order of 10^7, based on downstream distance) and small scales (typically 1 m or less), and the proper scaling laws remain unclear. For practical application of BDR to full-scale ships, experimental results at large scales and high-Reynolds numbers approaching those of full-scale craft are required.

High-Reynolds-number experiments on BDR were reported by Sanders *et al.* (2006) for a near-zero pressure gradient TBL. They showed that significant levels of BDR could be achieved near the injection location. However, they also reported that there was limited persistence of the BDR beyond a metre or two from the injection location. With such a short persistence distance, BDR is impractical for many applications because it would entail many gas injection locations and large volume fluxes of gas. Workers have speculated that the gas injection process can be optimized to minimize pumping requirements and improve BDR persistence, as the geometry of the injector will influence the size and speed distributions of the injected gas bubbles.

Sanders *et al.* (2006) also observed that, at lower flow speeds and higher gas injection rates, a layer of gas would form on the underside of the flat plate and persist along its entire length. Such air layers lead to skin-friction reduction of greater than 80 %. Air layers were observed for only a limited number of flow conditions, as examination of this phenomenon was not the principal goal of that study. However, persistent air-layer skin-friction drag reduction (ALDR) is a potentially important alternative to BDR. It was the major emphasis of the experimental study reported here.

This and the following paragraphs present a brief review of BDR and ALDR research. A seminal study of BDR was conducted when, using electrolysis to generate bubbles near the leading edge of an axisymmetric body, McCormick & Battacharyya (1973) showed promising results for skin-friction drag reduction. Net drag reduction approaching 40 % was observed on a body 0.91 m in length at flow speeds to 2.6 m s^{-1}. In another early study, Bogdevich & Evseev (1976) observed that drag reduction peaks immediately downstream of the point of injection; however, further downstream, skin-friction returned to its usual level. Since then, numerous BDR experiments have been conducted that investigated the parameters influencing drag reduction, some of which are described below. The relevant parameters include: downstream distance from the injector, gas flow rates, free-stream velocity, plate orientation (buoyancy), injector geometry, and surface roughness. A review of BDR can be found in Merkle & Deutsch (1992).

Workers at the Pennsylvania State University (PSU) have conducted a number of BDR experiments. For example Madavan, Deutsch & Merkle (1984*a*, *b*) measured drag reduction in a laboratory-scale flat-plate TBL. From these experiments they observed that: drag reduction was relatively independent of injector pore size (from 0.5 to 100 μm), bubble size distributions were determined primarily by the free-stream velocity and gas flow rate (increasing with increasing injection rate and decreasing free-stream speed), and drag reduction improves when the bubbly layer is beneath the solid surface of a plate rather than above it. Clark & Deutsch (1991) investigated drag reduction on an axisymmetric body with imposed pressure gradients. Their results showed that a mild favourable pressure gradient reduces the efficiency of BDR and that in adverse pressure gradients, gas injection leads to separation and high-levels of drag reduction. (Similar results were found by Kawakita & Takano (2000) where pressure gradients were applied to a flat-plate TBL with gas injection.) In addition, Fontaine & Deutsch (1992) used five different gases with varying density and solubility and showed that the type of gas has little or no effect on the observed drag reduction.

The influence of bubble size on BDR processes has been examined by several workers. McCormick & Battacharyya (1973) reported drag reduction of 10 % to 30 % with small bubbles generated by electrolysis, despite estimated mean void fractions in the boundary layer of the order of only 1 %. Kawamura *et al.* (2003) produced bubbles with two different methods: the first involved injecting air through a slot, producing bubbles from 0.5 to 2 mm in diameter. The second enlisted bubble formation through out-gassing to produce bubbles 1/10 to 1/100 the size of the injected bubbles. (As their test surface was beneath the TBL flow, this finding may be a result of the higher rise-velocity of the larger bubbles that causes them to migrate from the plate surface much more quickly.) They report that the smaller bubbles are nearly twice as effective at reducing skin-friction at equivalent void fractions. In contrast, Takahashi *et al.* (2001) examined BDR on a towed body and used surfactants to reduce the bubble size. They reported no apparent difference in the resulting drag reduction. The majority of BDR experiments have been conducted in fresh water. If bubble size is an important factor in drag reduction, equivalent flows of salt water would be expected to have a significant influence on the bubble sizes produced and the resulting levels of drag reduction. Winkel *et al.* (2004) showed that bubble formation is modified and the resulting size distributions are reduced by a factor of approximately four (in diameter) in salt water relative to fresh water. However, direct skin-friction measurements made by Shen, Perlin & Ceccio (2006) with gas injection into both fresh and salt water produced no measurable difference in drag reduction. In most studies of BDR, bubble diameters are much larger than the viscous length of the TBL, and it is possible that the injection of very small bubbles with dimensions of the order of the viscous length may lead to enhanced bubble–turbulence interactions and drag reduction. However, Shen *et al.* (2006) injected very small (of the order of $10\,l_\nu$, i.e. 10 viscous wall units) lipid-stabilized bubbles into the boundary layer and saw no measurable improvement in drag reduction compared to BDR flows with larger bubbles and equivalent void fractions.

A group of Japanese workers have performed experiments at large scales to address the issue of BDR scaling directly. Long slender flat-bottom ship models, ranging from 12 to 50 m in length, have been towed at speeds to $7\,\mathrm{m\,s^{-1}}$ with gas injection (Watanabe, Masuko & Shirose 1998; Kodama, Kakugawa & Takahashi 1999). The test models were very slender, with a beam/width of 0.6 or 1.0 m. Gas was injected over the centre 50 % of the model span. Drag reduction was observed to decay with downstream distance, and by the end of the 50 m model, only slight drag reduction

existed, of the order of a few per cent. Overall skin-friction reduction approaching 20 % on the 50 m model was reported. However, it should be noted that there were no 'skegs' or 'strakes' to contain the gas underneath the models, thus gas may have escaped from the sides of the vessel. Kodama *et al.* (2002) reported that drag reduction measurements made in the spanwise direction showed poor uniformity, decreasing from a maximum at the model centreline to nearly zero at the outer edges. This observation agrees with the concept of gas escaping from underneath the test models.

The same Japanese research group has attempted at least two BDR experiments on full-scale vessels exceeding 100 m in length. Gas was injected near the bow of a ship through horizontal arrays of holes at flow rates to $43\,\mathrm{m}^3\,\mathrm{min}^{-1}$. During the first at-sea demonstration (Kodama *et al.* 2000), no net power saving was observed. The researchers reported that, although skin-friction reductions were thought to have been achieved, an offsetting reduction in propulsive efficiency occurred because of gas entrainment into the propeller flow. In more recent at-sea demonstrations (Nagamatsu *et al.* 2002; Kodama *et al.* 2006), net friction reductions and power savings (after gas injection costs) of a few per cent were demonstrated. Owing to the scale and complexity (surface curvature, surface roughness and sloped surfaces) of these at-sea demonstrations, almost no details of the distribution (streamwise and spanwise) of the gas and corresponding drag reduction were measured.

The underlying physical mechanisms of BDR are not yet fully understood. It is generally agreed that for bubbles to reduce skin-friction they must in some way reduce the turbulent momentum exchange in the buffer region of the boundary layer. A number of different mechanisms have been proposed, and results suggest that multiple mechanisms work simultaneously. A reduction in the bulk density may play a role in the shear-stress reduction, by decreasing the Reynolds shear stresses, $-\rho\langle u'v'\rangle$, in the near-wall region. Moreover, if the drag reduction effect is due to a simple density reduction, the observed level of drag reduction should scale with the near-wall void fraction. Lumley (1973, 1977) hypothesized that the presence of bubbles locally increased the viscosity in the buffer region. This increase in local viscosity would then reduce turbulent fluctuation levels and increase the thickness of the sub-layer and buffer region of the TBL. Similarly, Pal, Deutsch & Merkle (1989) observed that not only did mean skin-friction levels decrease during gas injection, but fluctuations in skin-friction were suppressed. In contrast to the proposed reduction in turbulence levels, using Particle-image velocimetry (PIV) Nagaya *et al.* (2001) observed an increase in turbulent fluctuations with gas injection. Although increases in both u' and v' fluctuation components were observed during drag reduction, they de-correlated, effectively reducing the Reynolds shear stress. Finally, Meng & Uhlman (1998) propose 'bubble-splitting' as a mechanism for BDR. Their argument is that energy is extracted as a larger bubble is split into two or more bubbles; the surface area, A_s, increases resulting in a higher surface energy, γA_s, where γ is the surface tension.

Numerical simulations of bubbly turbulent flows have been conducted that also yield insight on the mechanism(s) of BDR at relatively low Reynolds numbers. Using direct numerical simulation (DNS) of a bubbly shear-layer, Druzhinin & Elghobashi (1998) showed that bubbles migrate to the vortex cores in a turbulent shear flow and reduce turbulent fluctuations. Lu, Fernández & Tryggvason (2005) examined bubbly channel flow and demonstrated the importance of bubble deformation whereby entrainment of bubbles into near-wall vortices suppressed the formation of streamwise vorticity and drag; this effect was not observed for non-deforming bubbles. Similarly, van den Berg *et al.* (2005) examined friction drag reduction in a Taylor–Couette

flow and also found a significant influence of bubble size and deformation on the bubble–vortex interactions and friction modification. These studies provide valuable insight into the scaling and mechanisms of BDR.

Though BDR has been studied extensively for more than 30 years, a universal scaling law that adequately collapses the experimental results has yet to be developed. The drag reduction is presented usually as a percentage drag-reduction, $\%DR$, where τ_{wo} is the shear stress without gas injection and τ_w is the (reduced) skin friction with gas injection:

$$\%DR = \left(1 - \frac{\tau_w}{\tau_{wo}}\right) \times 100. \tag{1.1}$$

We would like to know how $\%DR$ scales with the other independent parameters of the flow, such as the flow speed, U_∞, and the injected gas flux, Q_a, and other flow parameters. Madavan *et al.* (1985) report $\%DR$ as a function of the mean void fraction of air in the TBL, $\bar{\alpha}$, defined by (1.2)

$$\bar{\alpha} = \frac{Q_a}{Q_a + Q_W}, \tag{1.2}$$

where Q_W is the volumetric flux of the liquid through the unmodified momentum boundary layer defined by (1.3) where δ_{99} is the boundary-layer thickness, δ^* is the displacement thickness, and B is injector span,

$$Q_W = U_\infty B(\delta_{99} - \delta^*). \tag{1.3}$$

While this scaling can collapse data for a single set of specific experiments, it does not adequately collapse experimental data across different flows, as it neglects several parameters which influence bubble drag reduction.

Deutsch *et al.* (2003) and Sanders *et al.* (2006) suggest other scaling relationships for BDR on rough and smooth plates, respectively. They developed the scaling parameter

$$\frac{Q_a}{Q_a + U_\infty B\theta_0}\frac{u_\tau}{u_\tau^*} \tag{1.4}$$

for both rough and smooth plates, where θ_0 is the unmodified local momentum thickness, and u_τ and u_τ^* are the friction velocities of smooth and rough surfaces, respectively. Sanders *et al.* (2006) proposed a similar scaling law for BDR on smooth surfaces,

$$\frac{Q_a}{Q_a + U_\infty B(\theta_{0,inj} - \theta_0)}, \tag{1.5}$$

which produces a better collapse of the data. However, it should be noted that the improvement in the collapse is probably due to the reduction in the length scale, $[\theta_{0,inj} - \theta_0] < \theta_0$.

As opposed to BDR, ALDR occurs when a continuous or nearly continuous layer of air is formed between a solid surface and the outer liquid flow, as observed for a limited number of conditions by Sanders *et al.* (2006). Although few or no experimental investigations have been conducted specifically to investigate the ALDR phenomenon, BDR workers have inadvertently created and reported some of the characteristics of ALDR. Madavan *et al.* (1985) reported a maximum level of drag reduction, typically in excess of 80–90 %, where the increase of gas injection yielded little or no improvement in skin-friction reduction, probably associated with the formation of an air layer. Kodama *et al.* (2002) described an attempt to establish an air layer along a flat-plate test model at a free-stream speed of $10\,\mathrm{m\,s^{-1}}$. Although

	Test type	Model	Injector	Skin-friction measurement	Temperature (°C)
Test 1a	BDR	Smooth	Porous-plate and Slot A	Local	21.6
Test 1b	ALDR	Smooth	Porous-plate	Local	27.9
Test 2a	ALDR	Smooth	Slot B	Local	29.0
Test 2b	ALDR	Rough	Slot B	Local	22.0
Test 3	ALDR (inlet condition)	Smooth	Slot B (modified)	Integrated	22.2

TABLE 1. Summary of tests conducted and the experimental set-up employed for the BDR or ALDR experiments. The model surface condition, injector type, the method of skin-friction measurement, and mean temperature are given.

the exact gas injection rates were not described, no stable persistent air layer was established. They described an air film that persisted 20 cm downstream of injection, and subsequently separated into slugs of air that eventually evolved into bubbles further downstream.

In the present work, we continue the study of BDR and ALDR using the test model employed by Sanders *et al.* (2006) in an effort to understand the mechanisms underlying the limited persistence of BDR and the onset conditions for ALDR. In addition, the experiments reported here examined the influence of surfactants and surface roughness on the observed levels of drag reduction for both BDR and ALDR. The remainder of this paper is organized as follows: § 2 describes the experimental methods and the extent of the tests; § 3 presents the results along with a discussion of the scaling of BDR and ALDR; and § 4 provides a summary of this work and the conclusions drawn from it.

2. Experimental methods and the experimental program

Three separate tests were conducted in the US Navy's William B. Morgan Large Cavitation channel (LCC) on the same test model, and table 1 provides a summary of the experimental set-ups. (For a complete description of the LCC facility and its use, see Etter *et al.* 2005.) The schematic of the test model working surface for the primary experiment, Test 1, is shown in figure 1. The two additional ALDR experiments investigated surface roughness (Test 2) and inlet condition sensitivity (Test 3). Test 2 used the same layout as shown in figure 1 without the near-wall imagers and electrical impedance probes. Test 3 included a 1 cm step at the injector that was faired upstream to the model nose; the shear stress was integrated over sections of the body using six load sensors spanning nearly the entire model length. The coordinate system for these experiments has its origin located in the plane of the plate's leading edge with X increasing downstream, Y increasing normal to the test surface of the model ($Y = 0$ on the model's surface), and Z the spanwise coordinate. The suite of measurement devices included skin-friction force balances, *in situ* remote-controlled laser illumination for onboard photographic imagers, electrical impedance probes and air-flow metering. Bubble-image and electrical-impedance measurements were made in the near-wall region of the test model.

2.1. *Instrumentation*

2.1.1. *Gas injectors and flow metering*

Gas was injected through the lower surface of the test model at two locations, $X_{inj} = 1.38$ and 3.73 m, where X_{inj} is the injector downstream location. Two different

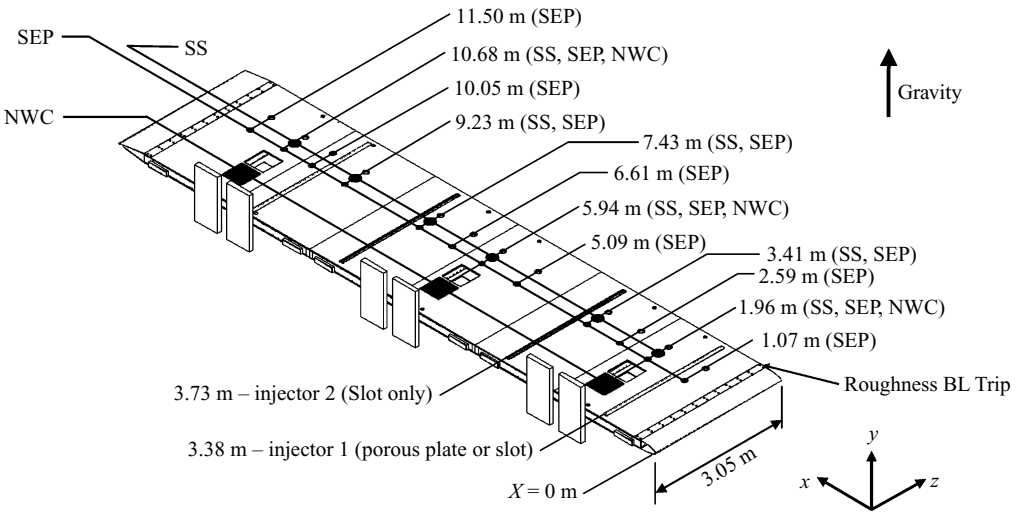

FIGURE 1. Schematic of the test model's working surface showing the injectors and instrument layout for Test 1. Gas injectors are located 1.38 and 3.73 m from the model's leading edge. Six skin-friction force balances and twelve surface electrical impedance probes are positioned in the streamwise direction. Near-wall imagers are positioned at $X = 1.96$, 5.94 and 10.68 m. SS, skin-fraction sensor; NWC, near-wall camera; SEP, surface electrical impedance probes.

types of injectors (slot and porous-plate), spanning the centre 2.65 m of the test model (∼87 % of the model span) were tested; cross-sectional schematics of the porous-plate injector can be found in Sanders *et al.* (2006) and the slot injector used in Test 1, Slot A, is shown in figure 2. The porous-plate injector consisted of a slot inclined at a mean angle of 25° from the model test surface and contracting at a full angle of 10°. The slot was capped by a layer of porous (40 μm mean pore diameter) sintered stainless steel (Mott Corporation), 2.0 mm thick extending 25 mm in the streamwise direction. The layer of sintered metal was flush with the model working surface and fastened to the injector to ensure that all injected air passed through the porous material (Sanders *et al.* 2006). Slot A was inclined 12° from the working surface with a constant throat gap of 5.75 mm that produced an opening in the streamwise direction of 28 mm. Tests 2 and 3 used the Slot B design, also shown in figure 2, which had the slot inclined at a shallow 5.7° from the model surface and contracting at a full angle of 6.1°. The downstream edge was broken, giving it a convex surface which produced a 15 mm opening on the test model surface. During Test 2, a porous material was used in the contracting slot to produce pressure drop close to the surface opening (required for a separate experiment not reported here). Test 3 used a modified injector from Test 2 with a 13 mm step affixed to the upstream edge of the injector opening. The injector opening was 1.4 m downstream of the leading edge of the plate. The step was constructed of PVC and continued forward to the nose of the model where it was faired with fiberglass reinforced epoxy. The injector from Test 2 was modified slightly with the installation of nine equally spaced vanes in the injection slot to maintain its shape. Two of these vanes, along with the previously installed baffles and screens, divided the injector into three sections. Each of these sections had its own manifold as well as airflow regulation (as described below).

The gas injection rate was monitored using two insertion thermal mass-flow meters (640S Steel-Mass, Sierra Instruments) mounted at the centre of a 6.3 cm inner diameter straight steel pipe. To ensure that the flow was fully developed at the monitoring

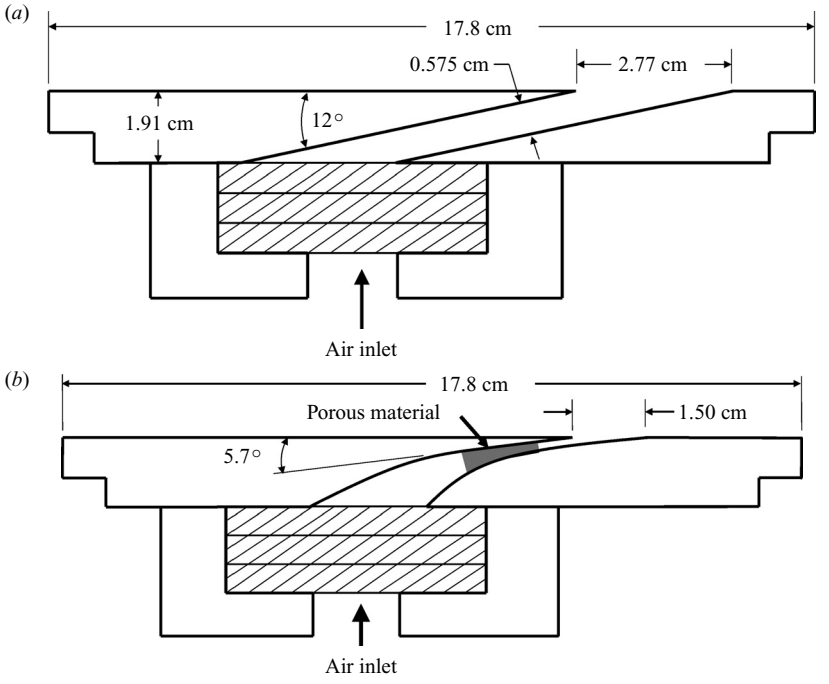

FIGURE 2. Cross-sectional schematic of (*a*) Slot A used during Test 1 and (*b*) Slot B used during Test 2. Test 3 used the lower injector without the porous material in the slot and a slightly modified air delivery system. Gas was distributed to the injector through 40 – 12.8 mm diameter ports evenly spaced along the span of the injector manifold. Three layers of baffles and screens served to create a pressure drop and evenly distribute the gas along the injector span. See Sanders *et al.* (2006) for the screen and baffle specifications and the porous-plate injector schematic.

locations, the flow meters were located 30 inner diameters (1.90 m) downstream and 10 inner diameters (0.63 m) upstream of any line junctions. The flow meters were factory calibrated for the range of 0–820 *SCFM* or equivalently 0–23.2 *SCMM* (Standard $m^3\,min^{-1}$) over an operating range of 0–345 kPa and 10–54 °C. An analogue voltage signal from each flow meter was recorded simultaneously with the skin-friction data. Gas was delivered to the injectors via 40 ports evenly spaced along a manifold that spanned the rear of each injector. Inside the manifold, three layers of screens and baffles were employed to generate a pressure drop to ensure the even distribution and uniformity of gas flux along the injector span.

2.1.2. *Skin-friction force balances*

Local skin-friction measurements were made at six streamwise locations using floating-plate-type drag balances (figure 1). The sensors are a modified design of those used by the PSU group, but were fabricated in-house. The floating plates were 15.2 cm in diameter, 0.79 cm thick, and made of 17-4 PH stainless steel. Each plate was fixed rigidly to a beryllium copper flexure that was instrumented with a full Wheatstone bridge of semiconductor strain gauges. The drag balance and its housing were flush mounted using an eight-point levelling system. The annular gap between the housing and the floating plate was $60 \pm 20\,\mu m$. The sensors used are the same as those of Sanders *et al.* (2006) with slight modifications to prevent flow through the sensor. The semi-conductor strain gauges were excited using a Vishay

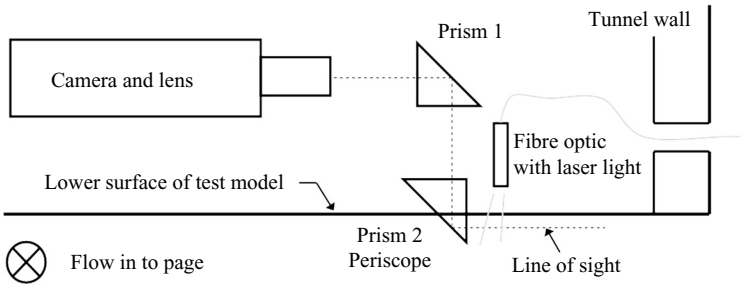

FIGURE 3. An elevation-view schematic of the near-wall imaging system used in Test 1. A periscope-type assembly of two prisms was used to deflect the camera line of sight to the near-wall region. The image area was illuminated from above using laser light delivered with a fibre optic cable. Not to scale.

signal-conditioning amplifier (Model 2310, Vishay Measurement Group). The sensor outputs were amplified and low-pass filtered at 10 Hz with the same Vishay unit. The output signal was recorded at 50 Hz with a National Instruments NI-DAQ data acquisition board and a LabView virtual instrument.

The skin-friction balances were calibrated *in situ* with loads ranging from zero to 8.9 N. The loads were applied to the floating plate *via* a suction cup affixed to the plate and a tensioning cable attached to a precision load cell (Model LCEB-5, Omega Engineering). Tension was applied to the cable by moving the precision load cell with a linear traverse. Such a set-up was necessary to eliminate biases that were found if the weights were simply suspended with cables and pulleys. The precision load cell was calibrated in the vertical position using laboratory weights prior to its use. Multiple calibrations were performed on the skin-friction sensors to confirm their repeatability and to assess their uncertainty. The measurement uncertainty was typically $\pm 5\,\%$.

Test 3 used a different set-up which measured the integrated skin friction over six sections (approximately 1.6 m^2 each) spanning the entire model length. To accomplish this, precision rails and linear bearings were used to affix the model skin to the body of the model. Each of the six sections was instrumented with force transducers/load cells to measure the total frictional force on the respective section.

2.1.3. *Bubble imaging systems*

Images of the near-wall gas-laden boundary layer were acquired using three monochrome $\frac{1}{2}$-in format CCD cameras (CV-M10-SX, JAI, 659×494 pixel resolution) with 50 mm focal length lenses (HF-50HA-1B, Fujinon) and 40 mm extension tubes at the streamwise locations shown in figure 1. To minimize blurring, the camera shutter speeds were set to 1.25 μs, creating a maximum image shift of less than two pixels ($<20\,\mu m$ in the streamwise direction) at the highest flow speeds. Images were acquired at 25 Hz with three analogue frame grabbers (IMAQ-1409, National Instruments) through a LabView interface. As much as 4 W of blue–green light from three different argon-ion lasers (Model 5300, Lexel; Innova I-90, Coherent; and Innova 70C, Coherent) were used to illuminate the field of view for the bubble images. The laser light was delivered to the viewing area using multi-mode fibre optics at each of the three streamwise locations.

A special technique was necessary to view the near-wall region. The image path used a periscope system consisting of two prisms with one prism protruding 5 mm from the surface of the test model. A cross-sectional schematic of the near-wall bubble imaging system is shown in figure 3. The image plane was normal to the

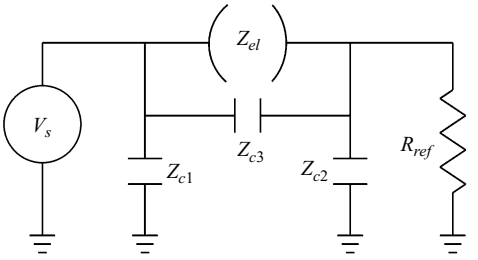

FIGURE 4. Circuit diagram of the electrical impedance probes used in Test 1. Shown is the voltage source, V_s, the impedance of the bubbly flow, Z_{el}, reference resistor, R_{ref}, and the stray capacitance from the lead wires Z_{c1}, Z_{c2} and Z_{c3}.

lower model surface and aligned with the flow. The imaging regions and scales were slightly different for each of the three near-wall cameras, but all were approximately 8 mm (streamwise) by 6 mm (vertical). The imagers were focused at the surface of the prism and the depth of field was measured to be 2 mm in air using a target inclined at 45° and noting where the image was in focus. It is noted that recorded bubble populations may be somewhat contaminated by the flow disturbance caused by the proximity to the protruding prism. The protruding prism was rigidly fixed within a machined slot in the model surface, which ensured that the surface of the prism, and thus the field of view, was aligned with the flow.

2.1.4. *Electrical impedance probes*

Electrical impedance probes were mounted on the model surface to measure the bulk void fraction in the near-wall region of the flow. (These measurements along with those from the near-wall cameras provided corroborative data regarding void fraction. Because of the difficulties involved with measurements of this type, redundant information was deemed necessary not just advantageous.) Each probe consisted of two brass electrodes soldered to signal conductors. The brass electrodes that were to be in contact with the flow were machined flush and mounted in an 11.4 cm diameter non-conducting flat PVC disk. Each disk had a large (3.2 mm diameter electrodes with 6.4 mm cross-stream separation) and a small (1.6 mm diameter electrodes with 3.2 mm cross-stream separation) electrode pair embedded. The purpose of the two sizes was to detect qualitatively void fraction gradients normal to the surface as illustrated in Cho, Perlin & Ceccio (2005). The probes were positioned 1.91 cm upstream and 1.91 cm downstream of the disk centre for the small and large probes, respectively. The disks were positioned slightly off the model's spanwise centreline and were centred at 12 streamwise locations ($X = 1.07, 1.96, 2.59, 3.41, 5.09, 5.94, 6.61, 7.43, 9.23, 10.05, 10.68, 11.50$ m). Each probe's interior surface was encased in an epoxy resin, which electrically isolated each electrode prior to contact with the flow.

The basic circuit for the electrical impedance probes is shown in figure 4 and consists of an a.c. excitation voltage (V_s), reference resistor (R_{ref}), probe electrical impedance associated with the flow (Z_{el}), stray capacitance from the input and output wires (Z_{c1} and Z_{c2}, respectively), and stray capacitance between the input and output wires (Z_{c3}). The stray capacitance between the input and output leads was minimized by shielding each separately, but it is included owing to its significant influence during measurement of higher void fractions. The input and output stray capacitance could not be neglected owing to the length of the wires required for the experimental set-up. This stray capacitance was measured *in situ* by short-circuiting the probe with

a known resistor and measuring the voltage V_{ref} across R_{ref}. The stray capacitance was measured repeatedly and showed negligible variation. The a.c. excitation voltage was produced with a signal generator (8904A multifunction synthesizer, HP), and the reference resistor had a nominal resistance of 75 kΩ, which maximized the output signal and sensitivity. Applying Kirchhoff's current law to the circuit provides the relationship between the electrode impedance and the known parameters:

$$Z_{el} = \frac{(V_s - V_{ref})R_{ref}Z_{c2}Z_{c3}}{V_{ref}[Z_{c2}(R_{ref} + Z_{c3}) + R_{ref}Z_{c3}] - R_{ref}Z_{c2}V_s}. \tag{2.1}$$

Four impedance measurement systems were fabricated to facilitate simultaneous measurements. During each experiment, measurements were acquired from each electrode pair, necessitating the use of a 128-channel multiplexer (PXI-2530, National Instruments) that was capable of switching between each set of four probes at more than 200 Hz. The sampling time for each probe was approximately 3 s; the data were acquired at 1000 Hz. After the start of a test, impedance-probe data acquisition was initiated once the skin-friction sensors reached steady state.

Increased probe sensitivity was achieved by recording the deviation of the measured impedance from the baseline (zero void fraction) impedance. A lock-in amplifier (LIA) (SR830 DSP LIA, Stanford Research Systems) and a signal generator (8904A multifunction synthesizer, HP) were used to excite and balance the bridge as well as to demodulate the resulting signal. The typical recorded output from the LIA was the amplitude and phase of $V_{ref} - V_w$ with a gain of 20, averaged over three ms, and band-pass filtered (0.01 Hz about the centre frequency), where V_w is the voltage across the reference resistor in pure water. Each circuit had a separate excitation frequency (5, 7, 9 and 11 kHz). A single computer controlled all the probe multiplexing, V_w amplitude and phase variation, and data acquisition via a LabView virtual instrument and data acquisition card (PCI-6040E, National Instruments).

2.2. *Data analysis techniques*

2.2.1. *Analysis of skin-friction drag reduction*

The drag reduction was computed directly from the measurements using (1.1). As gas was injected into the confined volume of the LCC, the static pressure in the test section increased and these pressure excursions led to baseline drift in the measured shear stress as well as changes in the injected volume flux of gas. To account for this, a time-record of the static pressure on the upper wall of the LCC test section was recorded simultaneously with the skin-friction and gas injection rate data. As BDR scales with the volumetric rate of gas injected into the boundary layer (Shen *et al.* 2006), the mass-flow rate recorded by the flow meters (as standard volumetric flow-rate) was converted to a true volumetric flow-rate at the test model surface using the ideal gas law. In addition, the increase in test-section pressure resulted in a decrease in the volumetric flow-rate. Thus, over the course of a gas injection test (typically 30–60 s) the volumetric injection rates decreased by as much as 30 % (dependent on the free-stream velocity and gas injection rate), which can have a significant effect on the level of drag reduction achieved. To account for this, the time traces of shear stress and volumetric gas injection rate were segmented into 0.5 s intervals. The drag reduction observed during each interval was divided into bins that were 0.3 $m^3\,min^{-1}$ in size.

2.2.2. *Near-wall void fraction analysis*

The region of influence of the electrode pair can be defined as the radial distance, R, from the model surface through which a nominal percentage of the current passes (Cho *et al.* 2005). Here the 'influence volume' is bounded by two arbitrary values of R/L (with L the electrode spacing), through which 50 % ($R/L = 0.85$) and 75 % ($R/L = 1.93$) of the electrical current flows. A value for R/L of 1.4 was selected, the average of the 50 % and 75 % values, which yield influence radii of 4.4 and 8.8 mm for the 3.2 and 6.4 mm electrode pair spacing, respectively.

The measured impedance of (2.1) can be related to the volume averaged void fraction, α, using Maxwell's mixture model, (2.2) (Ceccio & George 1996). This model provides an estimate only since the analysis of Hewitt (1978) following Maxwell (1881) assumed a uniformly disperse bubbly mixture, which is not expected in the present experiments.

$$\alpha = \frac{(Z_m - Z_w)(2 + \sigma_g/\sigma_w)}{(2Z_m + Z_w)(1 - \sigma_g/\sigma_w)}. \tag{2.2}$$

Here, Z_m and Z_w are the impedance of the mixture and water, respectively. σ_g ($\sim$0) and σ_w are the electrical conductivity of the gas and water, respectively. For the present study, the complex part of the mixture impedance is assumed to be negligible since $\sigma_w \gg 2\pi f \tilde{\varepsilon}_L \varepsilon_o$, where σ_w is the conductivity of water ($\sim$3.5 μS cm^{-1}), f is the input frequency ($\sim$10 kHz), $\tilde{\varepsilon}_L$ is the non-dimensionalized permittivity of the water ($\sim$80), and ε_o is the permittivity of a vacuum (8.85×10^{-12} F m^{-1}) (George, Iyer & Ceccio 2000). The real part of the mixture impedance (i.e. the conductivity) dominates when σ_w is greater than 0.44 μS cm^{-1}. The system was designed to measure the void fraction in bubbly flows, and as a result the void fraction measurements above 50 % (i.e. with an air layer) are only qualitative. Thus, void fraction measurements are not reported when an air layer is present; however, the impedance measured between the electrode pairs was large compared with bubbly flow measurements, indicating that the near-wall region was primarily air.

2.2.3. *Bubble population measurements*

The resolution in the near-wall video images ($Y \sim 0$ to 5 mm) was determined from images of a scale recorded periodically throughout the test. The image resolutions from the three near-wall cameras ($X - X_{inj} = 0.58$, 4.56 and 9.30 m) were determined to be 10.9 ± 0.2 12.0 ± 0.2 and 12.5 ± 0.2 μm pixel^{-1}, respectively. The stated uncertainty in the resolutions is the 95 % confidence interval determined from four different image calibrations and the Student's t-distribution.

The images used for the bubble populations were selected at random and analysed using National Instruments Vision Assistant program. The 'measurement tool' of this data analysis software was used to draw line segments across the (approximate) diameter of the near spherical bubbles, in the streamwise direction. Only in-focus bubbles were tabulated using a method described in Sanders *et al.* (2006).

Approximately 1000 total bubbles were counted from as many as 10 images for each flow condition. This is a sufficient number of bubbles to provide an accurate representation of the test data as the histograms are consistent on an image-to-image basis. An effort was made to count all the in-focus bubbles in each image to eliminate any random error; the worst possible bias error is estimated at two pixels ($\sim$25 μm) for the detection of each edge of the bubbles. This provides a bound on the smallest detectable bubbles in the images, about 25 μm, and while

bubbles smaller than one pixel might appear as specks in the images, this was not observed.

The physical size of the bubbles observed in the image analysis ranged from approximately 25 to 1000 μm. The resultant bubble diameters were placed in 25 μm bins. The bubble size distributions, $N(d)$, were normalized such that $\sum_{i=1}^{L_d} N(d_i) = 1$, where L_d is the number of bins and i is the bin index.

2.3. *Experimental program*

2.3.1. *Experimental test matrix*

In Test 1, the free-stream liquid velocity, gas injection rate, injection location, background surface tension and injector type were varied. Free-stream speeds ranging from 6.7 to 20.0 m s^{-1} and gas mass flow-rates of 100 to 800 *SCFM* (2.83 to 22.7 *SCMM*) with a maximum volumetric flux of 0.14 m^2 s^{-1} per unit injector span were tested. These experiments investigated BDR and ALDR from a single injection location, possible synergistic effects produced from compound injection from two slot injectors 2.35 m apart in the streamwise direction, and the influence of background surface tension on BDR and ALDR. To test this latter effect, the LCC background water surface tension was reduced from about 70 to 50 dyn cm^{-1} by adding 15 *w.p.p.m.* of a common soluble surfactant, Triton-X-100. Winkel *et al.* (2004) showed that the addition of surfactant to the tunnel volume can reduce mean bubble diameters by more than a factor of two immediately downstream of injection. However, this phenomenon was not observed in the current results, which indicates that it is limited to near the injector.

Test 2 investigated ALDR on a roughened surface in two parts: Test 2a repeated a subset of conditions from Test 1b to determine sensitivity to injector design. Then, in Test 2b the entire model surface was roughened using epoxy paint (High Build Semi-Gloss 97–130, Aquapon) with glass bead grit. The particles were packed tightly, producing a sand grain type roughness. Based on the skin-friction measurements and assuming a fully roughened surface, the leading 75 % of the model was very uniform yielding an average roughness height, k, between 400 and 600 μm. The remaining 25 % of the model was rougher with k ranging from 800 to 1100 μm. Free-stream speeds ranging from 6.7 to 15.8 m s^{-1} and volumetric air fluxes from 0.03 to 0.14 m^2 s^{-1} per unit injector span were tested.

Test 3 investigated ALDR via an alternative drag measurement method, and the effect of injecting air (sheltered immediately upstream by a small step) to mitigate the effect of large turbulent structures at the injection point. Six large (1.6 m^2) floating plates were used to measure integral drag on the plate, as opposed to the six small floating balances used previously. Free-stream speeds ranged from 5.9 to 11.8 m s^{-1} and gas injection rate per unit injector span varied from 0.049 to 0.16 m^2 s^{-1}.

For all drag-reduction experiments, prior to each injection a baseline (non-injection) skin-friction measurement was made for a period of about 15 s. For an injection run, shear stress data acquisition was started 5 s prior to gas injection and stopped 5 s post injection. In addition to the shear stress measurements, the gas mass flow-rate to one or both injectors and the static pressure of the LCC test section were recorded simultaneously. A control valve was preset to provide a desired gas injection rate according to the pre-determined test matrix. Two manually operated 10.2 cm diameter vents were added to the top of the LCC test section to help regulate pressure rise in the test section during a gas injection run. While the vents improved the pressure control, variations remained, and some pressure rise was recorded during gas injection.

2.3.2. *Comparison with the set-up and methods of Sanders et al.* (2006)

The results presented aim to extend and improve the data set collected from a first phase of BDR tests, see Sanders (2004) and Sanders *et al.* (2006). Tests 1a, 1b and 2a are meant to extend the current BDR research to larger scales, higher Reynolds numbers, and higher speeds in a well-controlled test environment. The previous phase of experimentation investigated drag reduction using injection from a single porous-plate injector located either 1.3 or 9.8 m downstream of the leading edge. Winkel (2007) provides additional information about Test 1, which investigated: (i) the influence of injector geometry; (ii) the influence of compound injection via simultaneous injection from two slot injectors ($X = 1.38$ and 3.73 m) for a variety of injection conditions; and (iii) the influence on BDR due to a reduction in surface tension from the addition of a soluble surfactant. Both experiments investigated similar ranges of flow speeds, from 6.7 to 20.0 m s^{-1}, and gas injection rates to 22.7 *SCMM*.

In addition to the different set of test parameters, the present experiment provided higher fidelity measurements than those of Sanders *et al.* (2006). The main improvements are in the control of tunnel pressure through the addition of test section vents and simultaneous measurement of that pressure and the gas injection rate. As gas was injected from the test model, the vents were controlled manually to allow air and water to be purged from the tunnel to accommodate the injected volume of air. Secondly, the accuracy of air injection rate and tunnel pressure were improved by recording the time traces of gas flow-rate with the skin-friction balances, whereas for Sanders *et al.* (2006), static pressure and air flow-rate were monitored visually from a digital display. The improved measurements of the present experiments allow for real-time comparison of drag reduction with volumetric gas injection rate. Lastly, the Sanders *et al.* ALDR results are extended with details of the onset conditions dependence on flow speed, surface tension, surface roughness (Test 2b) and inlet flow (Test 3).

3. Results

The presentation of results is divided into three subsections: non-injection (baseline) results; BDR results; and ALDR results. The BDR and ALDR results are separated as they are fundamentally different flow morphologies, though air layers can arise as a consequence of bubble injection. These subsections are further divided according to our principal findings, including the effects of various parameters and the examination of potential scaling methods.

3.1. *Baseline results*

3.1.1. *Smooth model baseline flow*

Figure 5 provides the non-injection skin-friction coefficients from Tests 1 and 2a on the smooth model, where $C_{fo} = \tau_{wo}/(1/2)\rho U_\infty^2$, and table 2 gives other baseline parameters from Test 1. Also plotted with the current baseline results are the best-fit curve from Sanders *et al.* (2006) and the Schultz-Grunow (1941) curve:

$$C_{fo} = 0.370 \log^{-2.584}(Re_X), \tag{3.1}$$

where $Re_X = U_\infty X/\nu$, X is the distance measured from the leading edge of the test model, and ν is the kinematic viscosity. It should be noted that Sanders *et al.* (2006) suspected their absolute skin-friction measurements were biased low owing to both calibration bias from pulley friction and possible flow through the sensor housing.

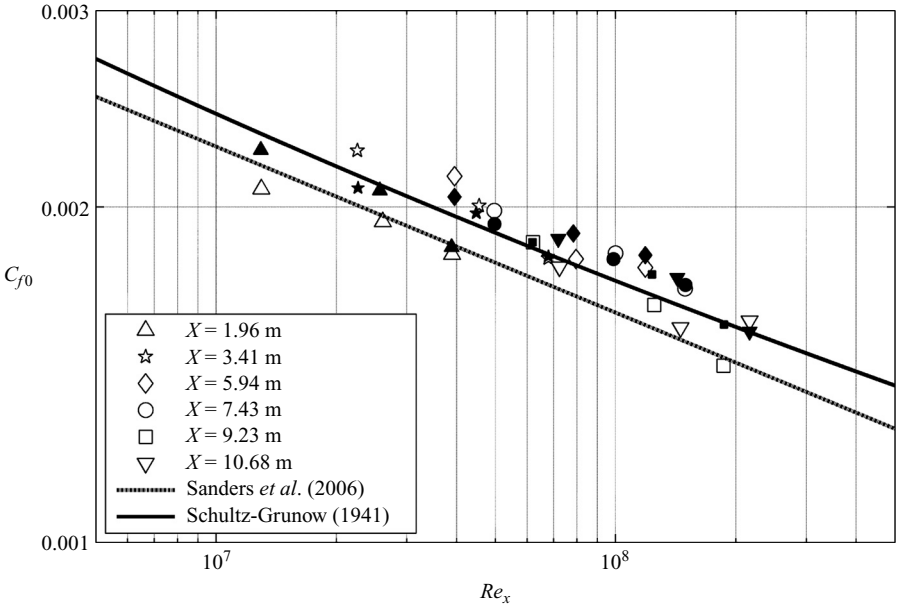

FIGURE 5. Baseline results obtained from Test 1 (solid symbols) and 2a (outlined symbols) on the smooth model at each streamwise measurement location. Also shown is the best-fit curve obtained by Sanders *et al.* (2006) on the same model and the Schultz-Grunow (1941) flat-plate skin-friction curve.

X (m)	U_∞ (m s^{-1})	τ_{wo} (Pa)	u_τ (m s^{-1})	l_v (μm)
1.96	6.60	48.9	0.22	4.5
1.96	13.1	178	0.42	2.4
1.96	19.8	362	0.60	1.7
3.41	6.65	45.9	0.21	4.7
3.41	13.2	171	0.41	2.4
3.41	19.9	357	0.60	1.7
5.94	6.65	45.1	0.21	4.7
5.94	13.2	165	0.41	2.5
5.94	20.0	360	0.60	1.7
7.43	6.70	43.2	0.21	4.8
7.43	13.3	158	0.40	2.5
7.43	20.1	344	0.59	1.7
9.23	6.71	41.7	0.20	4.9
9.23	13.4	155	0.39	2.5
9.23	20.2	320	0.57	1.8
10.68	6.73	42.3	0.21	4.9
10.68	13.4	154	0.39	2.6
10.68	20.3	317	0.56	1.8

TABLE 2. Baseline parameters for the smooth model of Test 1.

The current data were acquired after measures were implemented to eliminate these effects, as described above. The current results indicate that the Sanders *et al.* results were indeed biased low and that the present results from the same model are in good agreement with the Schultz-Grunow (1941) friction line. A more thorough reporting on the baseline TBL flow can be found in Oweis *et al.* (2008).

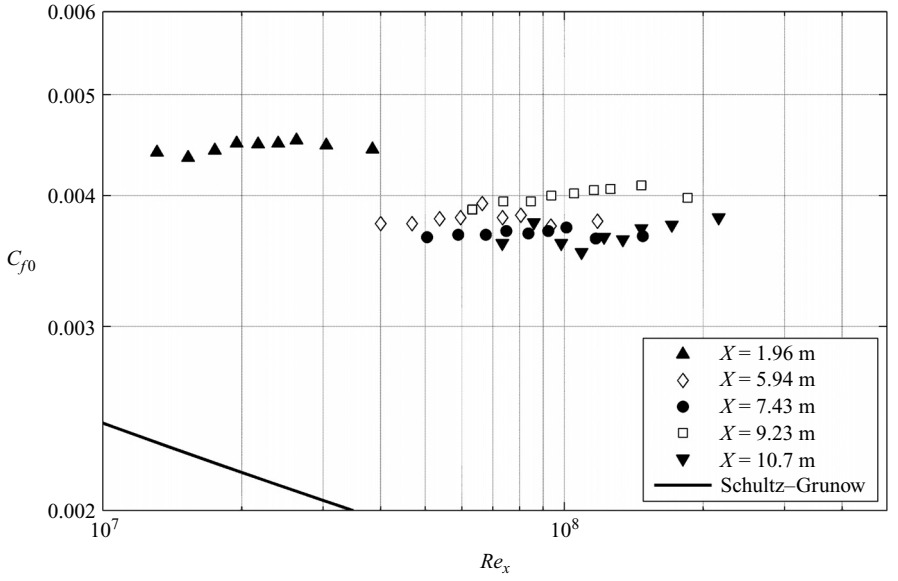

FIGURE 6. Baseline results from Test 2b on the roughened model surface. Data from each skin-friction balance are plotted separately ($X = 1.96$ to 10.7 m) to show the Reynolds-number independence. Also shown is the Schultz-Grunow (1941) curve that approximates the smooth-model baseline results.

3.1.2. *Rough model baseline results*

Figure 6 shows the non-injection results obtained from Test 2b on the roughened model surface. The particles embedded in the epoxy coating were packed tightly giving an average roughness height, $k \sim 460 \pm 120\,\mu$m. This k value was uniform across the leading 9 m of the plate; however, along the last 4 m, the coating was not applied as uniformly, resulting in approximately double the k value. These skin-friction coefficient curves were used also to estimate the average roughness height by assuming the surface is fully rough, which is supported by the Reynolds-number independence of the skin friction coefficient. The surface roughness was inferred from the measured drag after examining White's and Schlichting's friction curves for fully rough flow over a flat plate (White 1991). This method yielded average roughness heights of 400, 550, 580, 1100 and 830 μm at $X = 1.96$, 5.94, 7.43, 9.23 and 10.7 m, respectively. (Note for example that the $X = 9.23$ m position exhibits the second largest C_{fo} owing to its large roughness value.) These results are also consistent with a visual examination of the surface-embedded particles. These skin-friction results span a series of wall units from 1.1 μm at 15.8 m s^{-1} to 3.4 μm at 6.8 m s^{-1}.

3.2. *Bubble drag reduction*

3.2.1. *Down-stream persistence of bubble drag reduction*

Percentage skin-friction drag reduction, $\%DR$, is shown versus downstream distance from the injector ($X - X_{inj}$) in figures 7, 8 and 9 for the three primary test speeds ($U_\infty = 6.7$, 13.3 and 20.0 m s^{-1}). Both the porous-plate and slot-style injectors are shown with injection from the first injector ($X = 1.38$ m). Provided in the figures for each condition are the volumetric injection rates corrected for the static pressure in the test section. The keys indicate whether that condition corresponds to BDR, ALDR, or transition between BDR and ALDR. These regions are defined subsequently, but

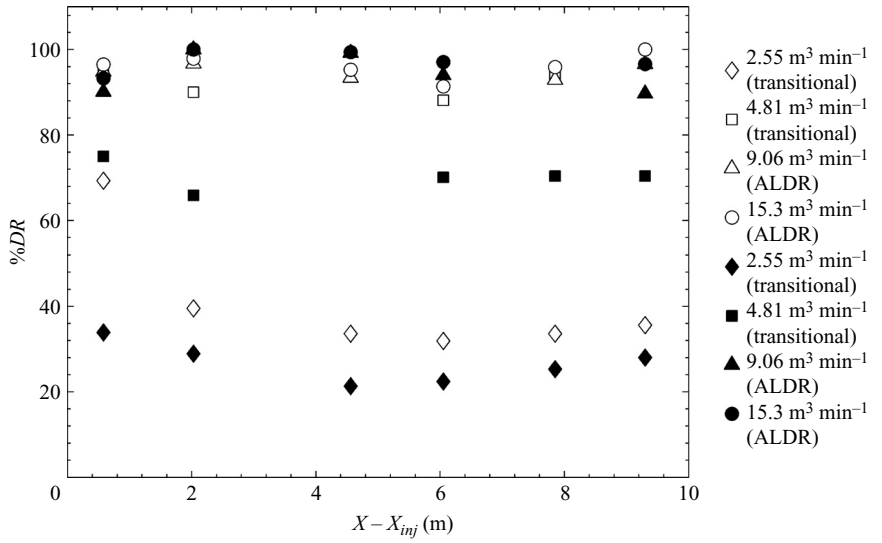

FIGURE 7. $\%DR$ versus $X - X_{inj}$ at a free-stream speed of 6.7 m s^{-1} during Test 1. A comparison of the Slot A (solid symbols) and porous-plate (open symbols) injectors at the four gas injection rates is presented. The key gives the volumetric gas injection rate corrected for test section static pressure, and in parentheses is whether this injection rate corresponds to BDR, ALDR, or the transition between BDR and ALDR.

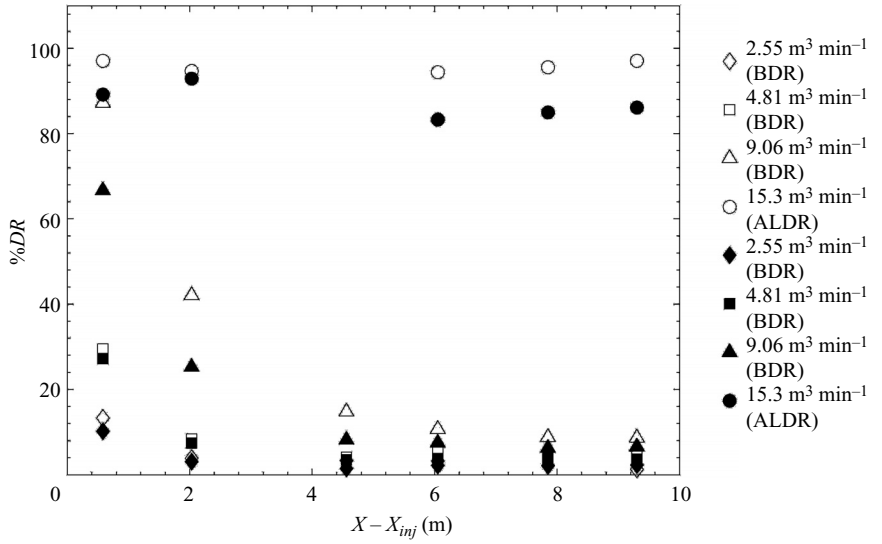

FIGURE 8. As figure 7, but for a free-stream speed of 13.3 m s^{-1}.

are provided here for clarity. For the current discussion of BDR, only the three lowest injection rates (2.55, 4.81 and 9.06 m^3 min^{-1}) at 13.3 m s^{-1} and all 20.0 m s^{-1} cases are used. Thus for the BDR conditions near the injector, high levels of drag reduction are observed and are then seen to decay rapidly with downstream distance. The decreasing drag reduction with downstream distance is associated with the migration of bubbles from the near-wall region where they are effective at reducing drag. Shear-induced lift forces from the mean velocity gradients in the boundary layer coupled with turbulent

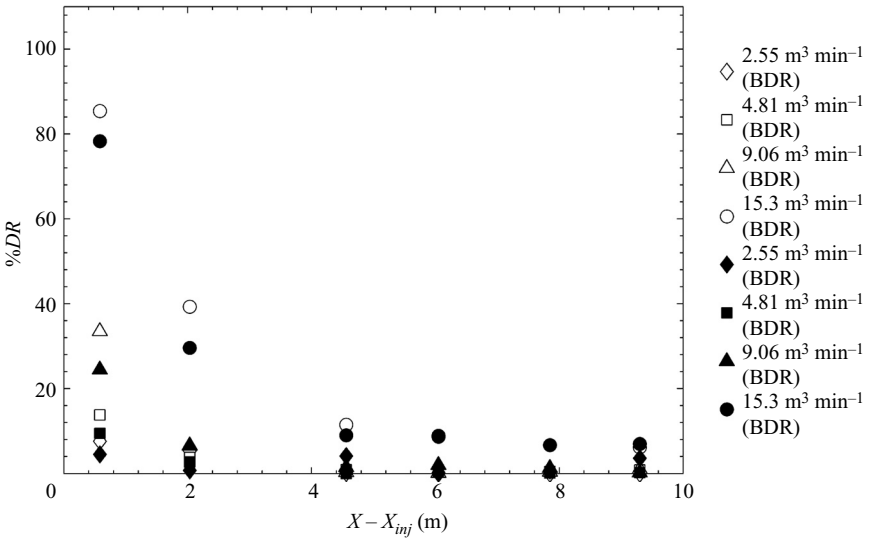

FIGURE 9. As figure 7, but for a free-stream speed of 20.0 m s^{-1}.

diffusion are suspected of driving the bubbles from the solid surface resulting in poor persistence of drag reduction. To demonstrate the shear-induced lift-force effect, simple models that map the trajectory of a single bubble in an unmodified TBL have been presented in Meng & Uhlman (1989) and Sanders (2004). Consequently, nearly all of the drag reduction was lost after the first 2 m at the higher flow speeds.

3.2.2. *Near-wall void fraction measurements*

Prior research has shown that gas distribution (void fraction) in the boundary layer during BDR has a peak occurring some distance (typically a few hundred wall units) from the wall (Merkle & Deutsch 1990). Furthermore, Pal *et al.* (1989) have reported that bubbles do not reside in the viscous sub-layer region, indicating that the void fraction asymptotes to zero at the wall. This near bubble-free zone in the near-wall region has been termed the 'liquid layer'. The existence of a liquid layer in our experiments is evidenced by the near-wall bubble imaging cameras; figure 10(*a*) shows a wall-normal image of the bubbly layer at $X = 5.94$ m and $U_\infty = 13.3$ m s^{-1} with 5.1 m^3 min^{-1} injection (where the measured drag reduction was about 10 %). The image shows a dark region immediately adjacent to the plate surface; the dark area indicates that there are few air–water interfaces (i.e. bubbles) to scatter the laser light and the mean near-wall void fraction determined with the electrical impedance probes under this condition was about 1 %. Conversely, figure 10(*b*) shows an image at the same location and speed but higher air injection rate (15.3 m^3 min^{-1}). In this image, the dark region is an air layer as supported by relatively large impedances between the electrode pairs. Note that because of impedance-probe design limitations, measurements above 50 % void fraction are not accurate and thus are not presented here.

Electrical impedance measurements also support the findings of Merkle & Deutsch, that the peak void fraction occurs away from the wall. Only the electrical impedance measurements on the plate surface at 20.0 m s^{-1} are included here. Void fraction estimates versus $X - X_{inj}$ are shown for the two electrode pair spacings (3.2 and 6.4 mm, i.e. small and large, respectively) in figure 11. At 20.0 m s^{-1} the void fraction

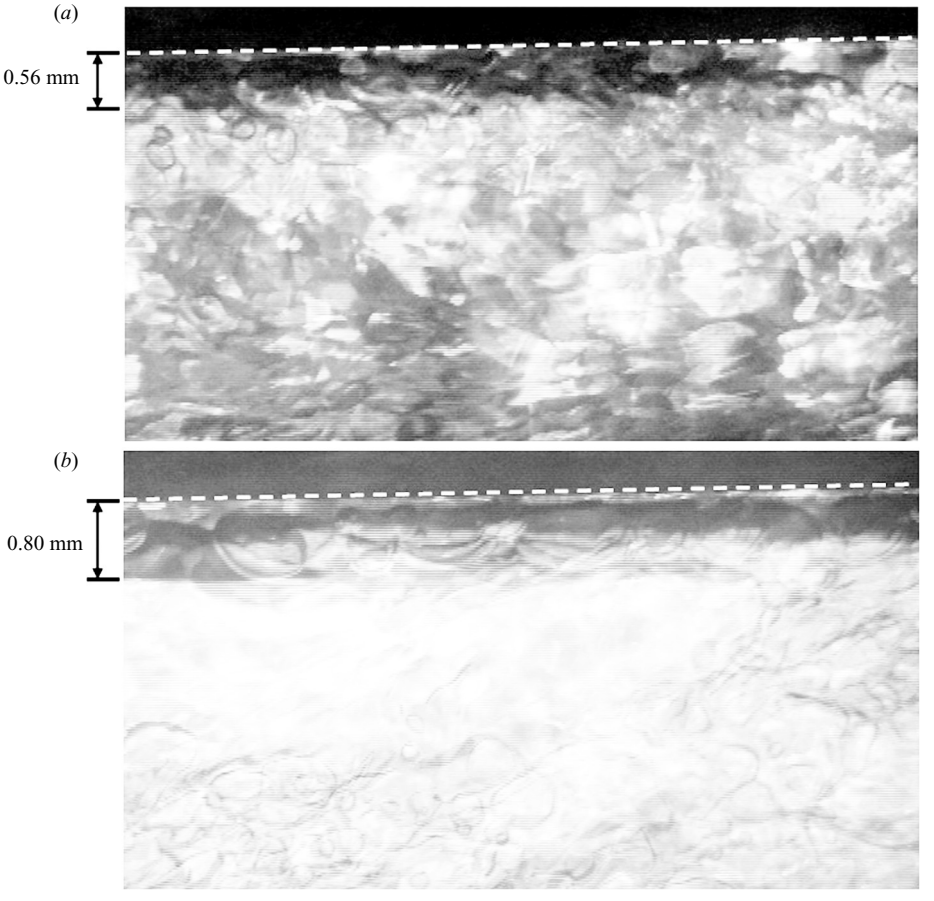

FIGURE 10. Photographic images of the near-wall bubbly flow at $13.3\,\mathrm{m\,s^{-1}}$ ($X = 5.94\,\mathrm{m}$) with (*a*) 5.1 and (*b*) $15.3\,\mathrm{m^3\,min^{-1}}$ injection from Slot A. The image is approximately 4.1 (wall-normal) by 7.7 (streamwise) mm, and the flow is from right to left. Both images have a dark region adjacent to the wall (region below the superposed white dashed line that represents the plate location) indicating that there are minimal air–water interfaces. (*a*) has a mean void fraction of 1 %, which indicates that the dark region is a liquid-layer. Conversely, (*b*) has large impedance measurements that prevented an accurate void fraction measurement, but the high impedance indicates that the dark region is primarily air.

measurements beyond the first 2 m were of the order of a few per cent. The void fraction measurements made by the electrodes with the larger spacing consistently show higher void fraction. The larger electrode spacing resulted in a larger 'influence volume' and therefore measured the impedance of a larger portion of the boundary layer. From this, we qualitatively infer that the void fraction increased with distance from the wall, as discussed by Cho *et al.* (2005). This result agrees with the results reported by Nagaya *et al.* (2001). In figure 12, the void fraction versus $X - X_{inj}$ is shown for the four nominal injection rates to compare the two-injector geometries and the addition of surfactant, all at $20\,\mathrm{m\,s^{-1}}$ free-stream speed. Similar results were obtained with the porous-plate injector with and without surfactant in the background, and the near-wall void fractions were consistently higher with the porous-plate injector than with the slot injector. This increase in void fraction is consistent with the mild improvements observed in drag reduction using the porous-plate injector. Skin-friction

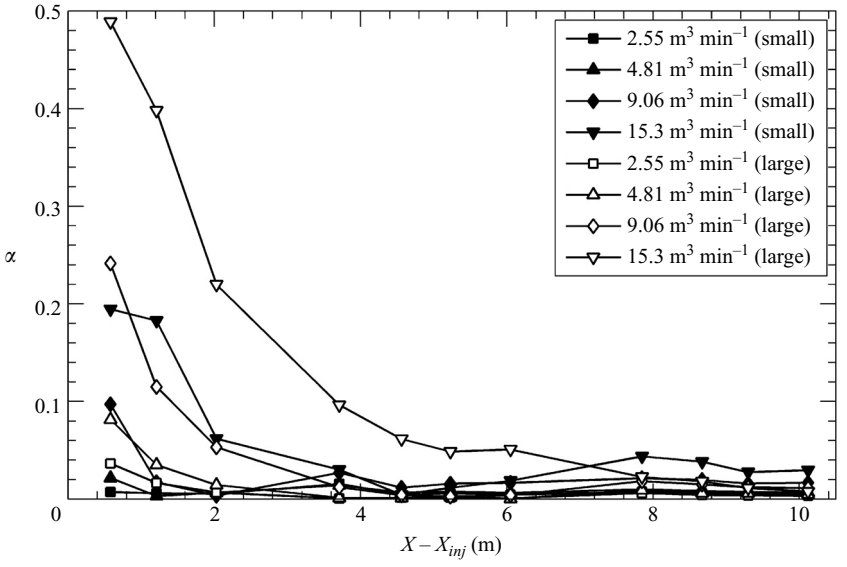

FIGURE 11. Near-wall void fraction, α, versus downstream distance from the injector at 20.0 m s^{-1} for the porous-plate injector (Test 1) measured by the surface electrical impedance probes for different gas flow rates (m^3 min^{-1}). Two electrode pair spacings are shown: 3.2 mm (small/solid symbols) and 6.4 mm (large/open symbols).

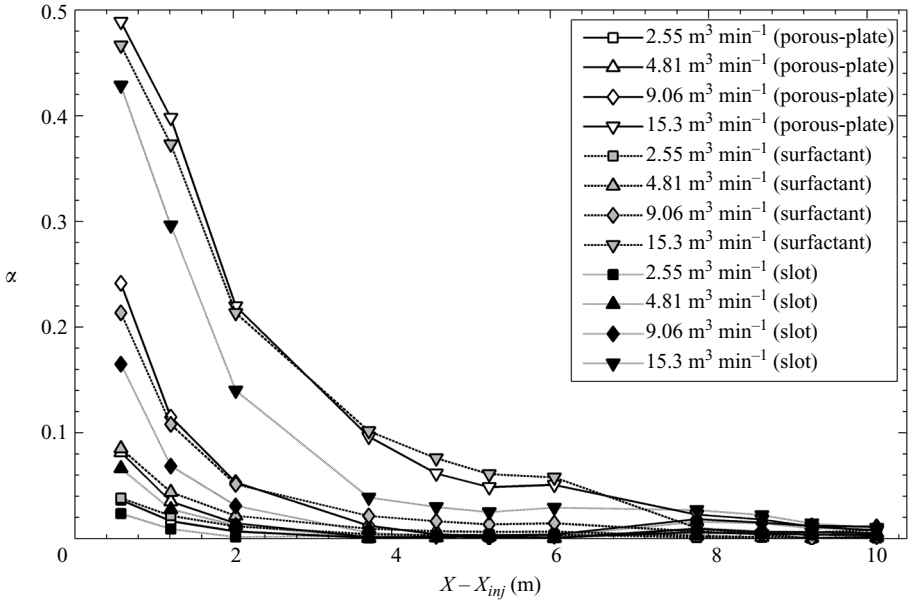

FIGURE 12. The near-wall void fraction, α, measured with electrical impedance probes versus downstream distance from the injector at the four nominal injection rates is shown for the porous-plate (with and without surfactant in the background) and upstream injection from Slot A without surfactant background. These data from Test 1 all correspond to free-stream speeds of 20.0 m s^{-1} and the large, 6.4 mm, electrode spacing.

drag reduction is shown in figure 13 as a function of the estimated near-wall mean void fraction measured by the impedance probes at 20.0 m s^{-1} for both electrode pair spacings. Both are reasonably well represented by a straight line with the smaller

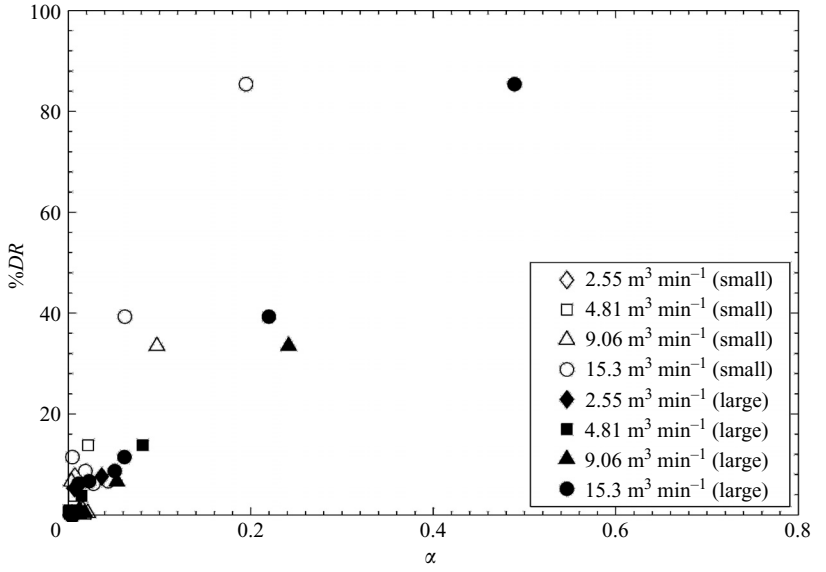

FIGURE 13. $\%DR$ versus α, the near-wall mean void fraction in the boundary layer measured by the surface impedance probes for the porous-plate injector at 20.0 m s^{-1} from Test 1.

electrode spacing having approximately twice the slope of the large spacing. This reinforces that bubble stratification away from the wall occurs near the plate surface.

3.2.3. *Scaling of bubble drag reduction*

The scaling laws developed from previous BDR research (described in § 1) are evaluated with the present data set. First, the scaling law developed by Madavan *et al.* (1985), which assumes that drag reduction is proportional to the mean void fraction, $\bar{\alpha}$, across the entire boundary layer is applied, and the results shown in figure 14 for the two injector styles. This scaling produces a rather poor collapse of the experimental results obtained in the present study. Secondly, the more recent scaling law developed by Deutsch *et al.* (2003) is implemented and the outcome is shown in figure 15, where the length scale employed is the momentum thickness, θ_0 rather than the boundary-layer thickness. Once more this scaling produces a rather poor collapse of the current data set.

To improve BDR scaling, we posit a new 'initial zone' scaling. Following Madavan *et al.* (1984*a*), we begin with drag reduction as a function of the dimensionless quantity,

$$\frac{Q_a}{U_\infty S}, \tag{3.1}$$

where S is the area through which the gas is injected. In their study, gas was not injected from a line source, but through the surface area of the plate spanning the tunnel width and 23 cm in the streamwise direction. This scaling is modified to represent a nominal air-layer thickness, t_a, given by (3.2) by assuming that the injected gas is moving at the free-stream velocity, where B is now the injector span rather than the area of gas injection:

$$t_a = \frac{Q_a}{BU_\infty}. \tag{3.2}$$

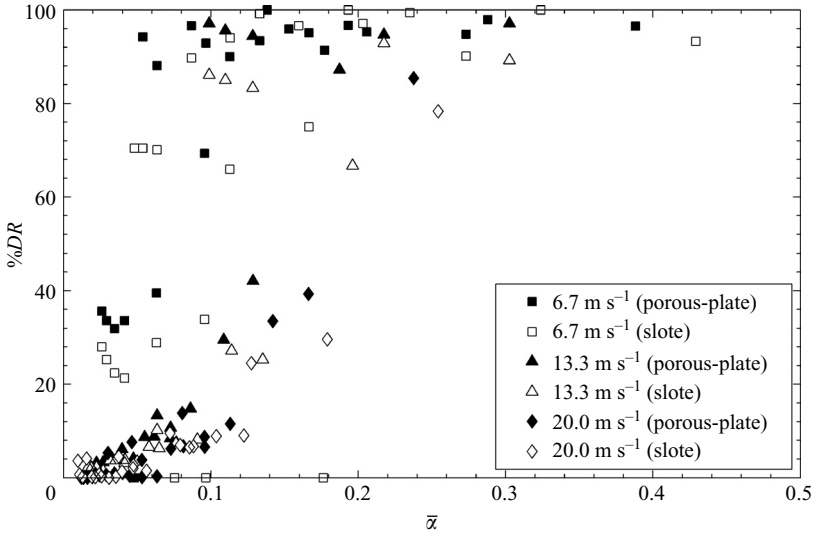

FIGURE 14. $\%DR$ versus $\bar{\alpha}$, the mean void fraction across the entire boundary layer, shown for the two injector styles and the three free-stream speeds from Test 1.

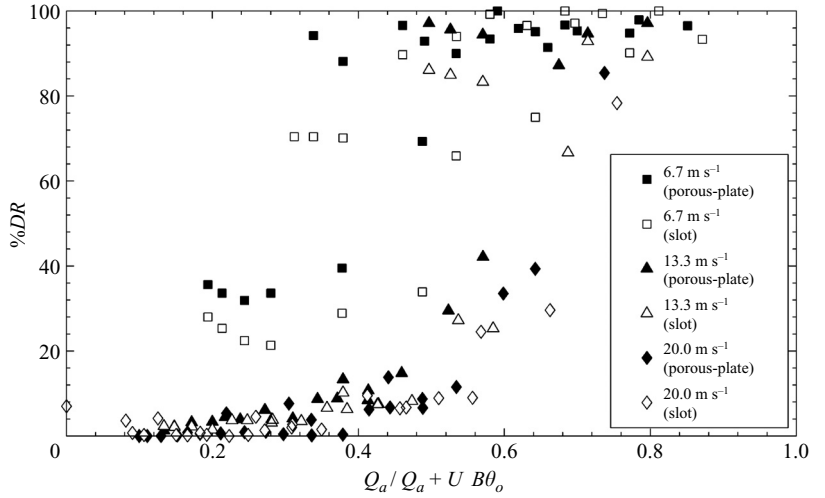

FIGURE 15. $\%DR$ versus the scaling of Deutsch *et al.* (2003), (1.4), for the smooth surface where $u_\tau = u_\tau{}^*$. Results are from Test 1 with porous-plate and Slot A injectors.

Drag-reduction measurements from the first shear-stress balance ($X - X_{inj} = 0.58$ m) are presented in figure 16 as a function of t_a. The present results show a fair collapse and agree well with the findings of Madavan *et al.* (1984*a*), whose results are also shown in figure 16. Although a reasonable collapse is evident near the point of injection, t_a fails to collapse the results from sensors further downstream (data not shown). Thus, this scaling yields no information about the downstream persistence of BDR.

3.2.4. *Bubble drag reduction with compound injection*

To investigate whether synergy occurs with nearby injection locations, experiments were conducted where gas was injected into the boundary layer simultaneously from

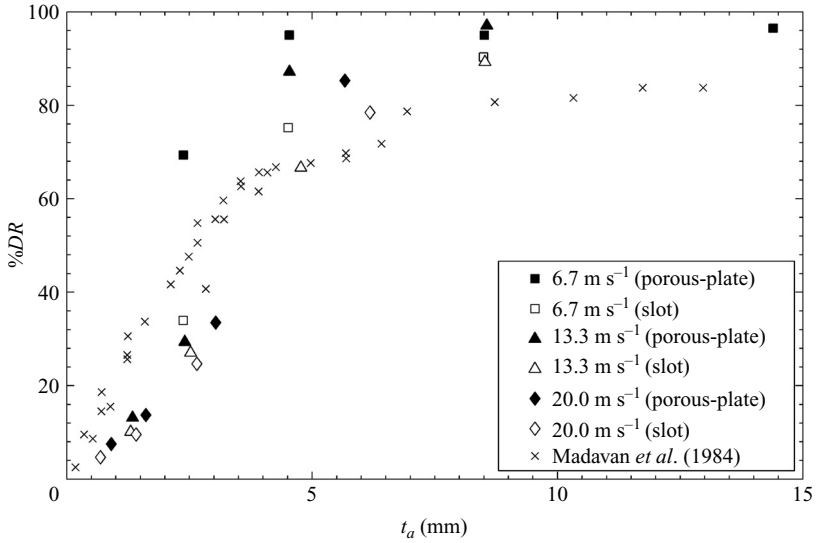

FIGURE 16. The first skin-friction balance ($X - X_{inj} = 0.58$ m) $\%DR$ versus an 'initial zone' scaling nominal air-layer thickness, t_a. Data are presented for the porous-plate and Slot A injectors (Test 1) along with the results of Madavan *et al.* (1984*a*), where $X - X_{inj} = 0.254$ m measured from the injector to the downstream edge of the drag balance.

two slot-type injectors spaced 2.35 m in the streamwise direction. Drag reduction was measured for a variety of nominal gas injection rates at the three nominal test speeds. Aggregate gas injection rates from both injectors were limited to 22.7 *SCMM*, the maximum flow rate of a single injector. To analyse the effect of compound injection on drag reduction, the sum of drag reduction achieved with slots 1 and 2 independently is compared with the drag reduction obtained with the same air flow rates using compound injection. In many cases, it was found that there was little difference between the two, such as shown in figure 17(*a*) with a total air flux of 9.6 m^3 min^{-1} at 13.3 m s^{-1}. However, figure 17(*b*) shows results at the same test speed (13.3 m s^{-1}) with a higher total air flux (18.1 m^3 min^{-1}) and a significant deviation between single injection and compound injection is observed. For the same aggregate injection rate, a single injector yielded much larger drag reduction than simultaneous injection from two slots. Here, injecting the full gas flux from slot 1, produced near 100 % drag reduction over the entire plate. This observation is a result of the transition from BDR to ALDR, which will be discussed subsequently. In contrast, no stable air film was formed when the gas flow rate was split evenly between the two injectors – the drag reduction decayed drastically – even if the total volume was larger than the single-injector case. These results indicate that there are no synergistic effects of compound injection that improve efficiency of BDR over the range of parameters investigated; rather, splitting the gas injection between two injectors can actually reduce the total drag reduction by preventing a transition from BDR to ALDR.

3.2.5. *Influence of injector geometry*

The skin-friction drag reduction results presented in figures 7 to 9 indicate that changes in the injector geometry as tested have only a weak effect on either the effectiveness or the downstream persistence of BDR. However, rather consistently at all speeds and injection rates, slightly higher levels of drag reduction were observed

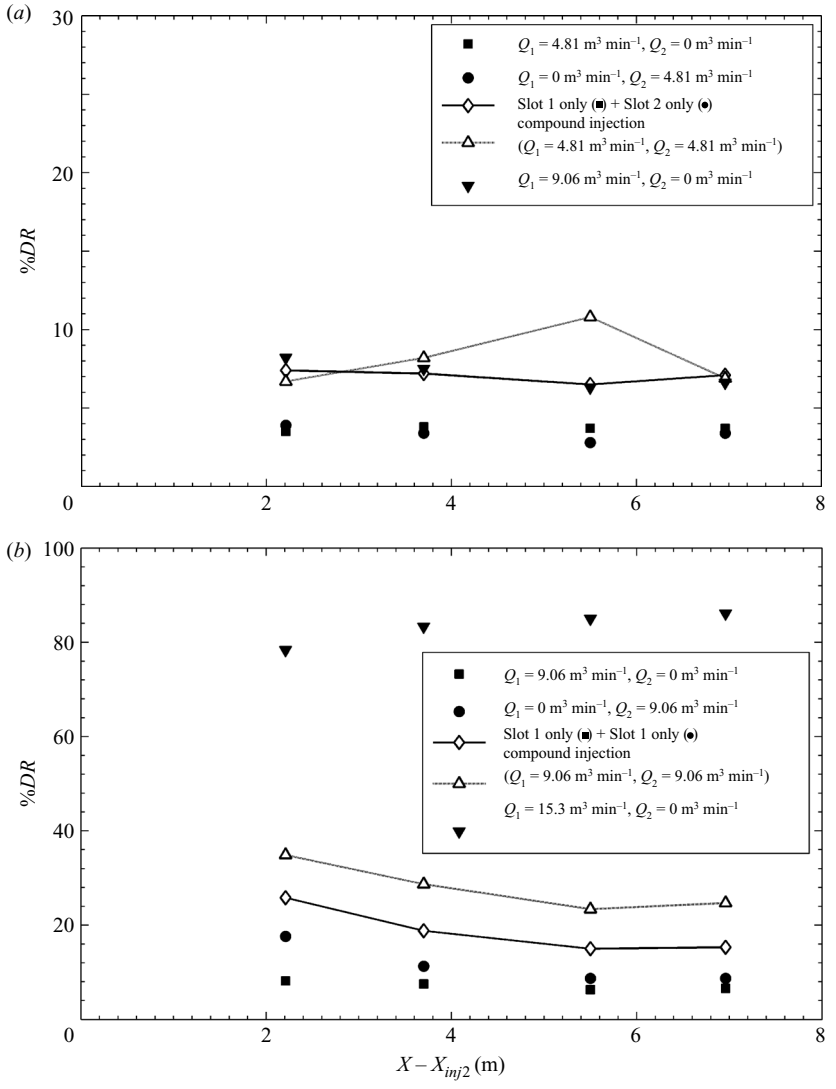

FIGURE 17. %DR obtained from Test 1 versus downstream distance from injector 2 ($X_{inj2} = 3.73$ m) at 13.3 m s^{-1} with gas injection from slot 1 only, slot 2 only, and simultaneously from both slots at (*a*) 4.81 m^3 min^{-1} and (*b*) 9.06 m^3 min^{-1}. For comparison with compound injection, solid lines that represent the simple sum of drag reduction from slots 1 and 2 only (i.e. from the filled squares and circles) are shown; dashed lines represent compound injection. Also shown is (*a*) 9.06 m^3 min^{-1} and (*b*) 15.3 m^3 min^{-1} injected only from slot 1. All slot injectors were Slot A type.

with the porous-plate injector than with the slot injector, although the differences lie within the uncertainty of the measurements. This result qualitatively agrees with the findings of Madavan *et al.* (1985), who showed that gas injection from porous-plate injectors with two different pore diameters (0.5 and 100 μm) showed measurable yet minor differences in drag reduction.

3.2.6. *Influence of surface tension on BDR*

To investigate the influence of bubble size on drag reduction, a surfactant was employed to reduce the surface tension and, in theory, the bubble size. A common soluble surfactant (Triton-X-100) was added to the background volume of the test

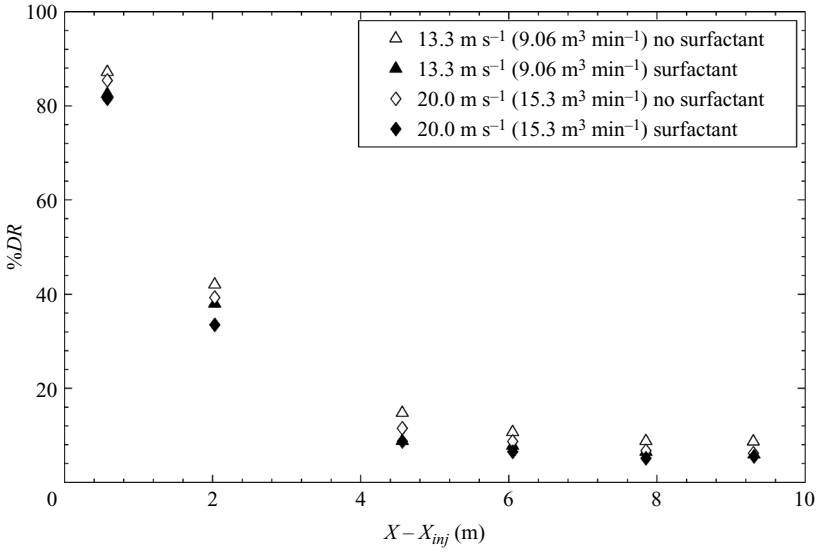

FIGURE 18. $\%DR$ versus $X - X_{inj}$ using the porous-plate injector with and without surfactant in the background. Results from Test 1 indicate negligible differences in drag reduction with the reduction in surface tension from 70 to about 50 dyn cm^{-1}.

facility at a concentration of 15 w.p.p.m. Winkel *et al.* (2004) showed that this can reduce bubble size by a factor of two, at least near the injector. The surface tensions of samples from the tunnel volume were measured with an *in situ* tensiometry device, which is described in Lapham, Dowling & Schultz (1999). The surface tension of the tunnel volume was measured to be 70 ± 1 dyn cm^{-1} prior to the addition of the surfactant and 50 ± 2 dyn cm^{-1} during testing. The surfactant employed has been shown to have time-dependent properties by Lapham *et al.* (2001), but repeated measurements during the surfactant test period revealed that a change of less than 3 dyn cm^{-1} occurred. Drag reduction at 13.3 and 20.0 m s^{-1} for the porous-plate injector, with and without surfactant in the tunnel volume, are compared in figure 18, exhibiting little significant difference in drag reduction. Although there was a measurable difference in surface tension, the bubble camera images showed little or no measurable reduction in bubble sizes (table 3) in the near-wall region, in contrast to the findings reported by Winkel *et al.* (2004) where measurements were made immediately downstream of injection. However, the observation that drag-reduction performance was unaffected by the addition of surfactant agrees with the findings of Takahashi *et al.* (2001). In addition, histograms of the bubble populations in the near-wall region at 20.0 m s^{-1} are shown in figure 19 for the 5.66 and 22.7 *SCMM* injection rates for the porous-plate, slot and surfactant (porous) injection tests. This shows that bubble sizes downstream from the injector are independent of injector design and background surface tension, and that the mean bubble diameters increase with increasing gas injection rate.

3.2.7. *Influence of boundary-layer thickness*

The influence of boundary-layer thickness on drag reduction at the line of injection is shown in figure 20, comparing the drag-reduction results for a single injection rate from either slot 1 ($X = 1.38$ m) or slot 2 ($X = 3.73$ m) at 13.3 and 20.0 m s^{-1}. Although the data points are sparse, the data appear to collapse, indicating that boundary-layer thickness at the line of injection may have minimal influence on the magnitude or

Upstream location, $X = 1.96$ m				
Injection rate	2.55 $m^3\ min^{-1}$	4.81 $m^3\ min^{-1}$	9.06 $m^3\ min^{-1}$	15.3 $m^3\ min^{-1}$
Sintered metal	123 μm	146 μm	130 μm	138 μm
Surfactant	135 μm	105 μm	N/A	N/A
Slot A	106 μm	133 μm	124 μm	178 μm
Downstream location, $X = 10.68$ m				
Injection rate	2.55 $m^3\ min^{-1}$	4.81 $m^3\ min^{-1}$	9.06 $m^3\ min^{-1}$	15.3 $m^3\ min^{-1}$
Sintered metal	80 μm	92 μm	90 μm	181 μm
Surfactant	76 μm	88 μm	94 μm	149 μm
Slot A	N/A	99 μm	99 μm	209 μm

TABLE 3. The mean bubble diameters measured with the near-wall bubble cameras ($Y < 5$ mm) at the upstream and downstream locations with a free-stream speed of 20.0 $m\ s^{-1}$. Bubble diameters are given for the porous-plate (sintered metal) injection, porous-plate injection with surfactant ocean and Slot A injection.

persistence of BDR. The ratio (slot 2/slot 1) of the boundary-layer thickness and friction velocities are approximately two and one, respectively. Therefore, while the boundary-layer thickness did change for the two cases, the resulting drag reduction was not influenced strongly. This challenges scalings based solely on outer variables, such as proposed by Madavan *et al.* (1985) and Sanders *et al.* (2006) where TBL thickness is a length used to scale $\%DR$.

3.3. *Air-layer drag reduction*

3.3.1. *The abrupt transition to air-layer drag reduction*

Under certain conditions, drag reduction approaching 100 % was achieved over the entire downstream length of the test model (approximately 10 m). This high level of drag reduction resulted from the formation of an air layer between the model and the liquid flow. The formation of an air layer is evidenced by dark images from the near-wall cameras as none of the laser light was scattered from air–water interfaces (see figure 10*b*), by the large impedance measured by the electrical impedance probes, and by qualitative images from an oblique view of the lower plate surface from outside the tunnel during Test 2b.

Sanders *et al.* (2006) achieved air-layer drag reduction for only a limited set of flow conditions. Reported here are the results from a series of experiments designed to investigate the conditions necessary to achieve air layers and hence ALDR. Experiments were conducted only for the porous-plate injector (with and without surfactant in the tunnel background) from the upstream location ($X = 1.38$ m) at four free-stream speeds, nominally 6.7, 8.9, 11.1 and 13.3 $m\ s^{-1}$. ALDR was not observed at speeds higher than 13.3 $m\ s^{-1}$ in this first set of experiments owing to the limitations in the capacity of the gas delivery and metering systems. (In § 3.2.3, additional experiments with surface roughness added are discussed and speeds to 15.3 $m\ s^{-1}$ are reported.) For each free-stream speed, the gas injection was varied slowly (approximately 0.142 to 0.283 $SCMM\ s^{-1}$) from zero using a manual control valve, until a maximum level of drag reduction was observed over the entire length of the test model. Once a maximum level of drag reduction was observed, the flow rate was decreased slowly to zero injection. No appreciable differences were observed

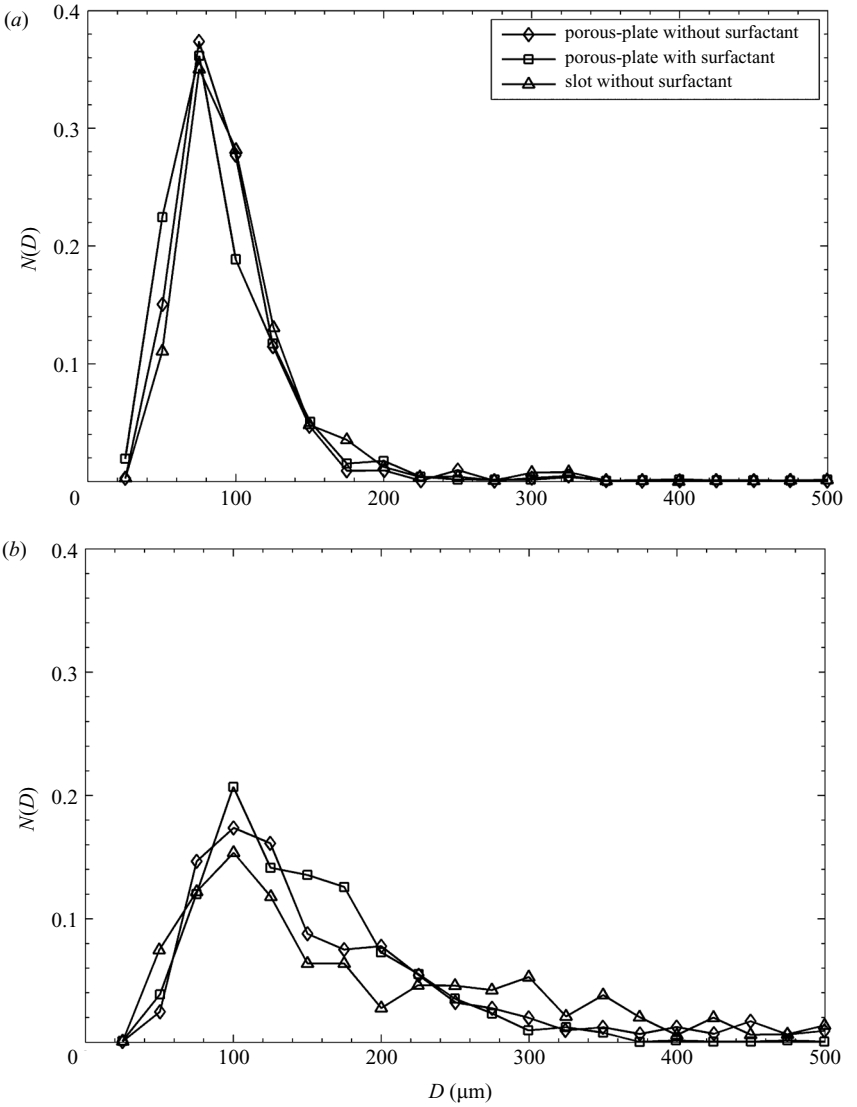

FIGURE 19. Bubble size distributions at $20.0\,\mathrm{m\,s^{-1}}$ free-stream speed with the porous-plate injector with and without surfactant and the upstream slot injector (Slot A) at ($X-X_{inj}=9.3\,\mathrm{m}$) for (*a*) $4.81\,\mathrm{m^3\,min^{-1}}$ injection and (*b*) $15.3\,\mathrm{m^3\,min^{-1}}$ injection. Data were collected from the near-wall bubble cameras during Test 1a.

in drag-reduction values when increasing or decreasing gas flow rates were employed, i.e. no hysteresis was observed.

From the varying injection rate experiments, $\%DR$ versus volumetric gas injection rate per unit span, q, curves were generated at a given flow speed. $\%DR$ versus q is presented in figure 21 for four sensor locations and a flow speed of $11.1\,\mathrm{m\,s^{-1}}$. As observed in BDR, over the lower-range of gas injection rates, $\%DR$ decreases with downstream distance. However, above a critical gas injection rate, q_{crit} (see figure 23), high levels of drag reduction were observed with no apparent decay with downstream distance over the entire downstream test surface.

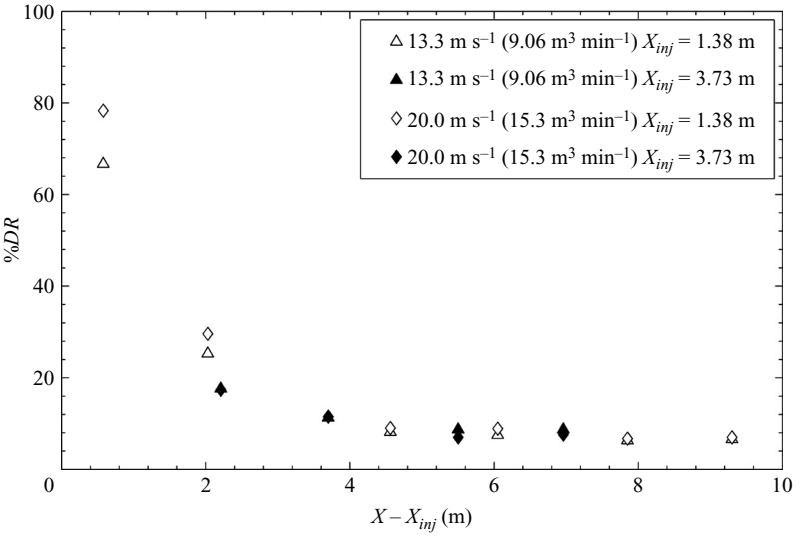

FIGURE 20. $\%DR$ versus $X - X_{inj}$ (m) from Test 1a from Slot 1 ($X_{inj} = 1.38$ m) or Slot 2 ($X_{inj} = 3.73$ m) at free-stream speeds of 13.3 and 20.0 m s^{-1}. Open symbols represent Slot 1 injection and closed symbols represent Slot 2 injection. Results indicate that boundary-layer thickness at the point of injection has little effect on drag reduction. Both slots used Slot A type injectors.

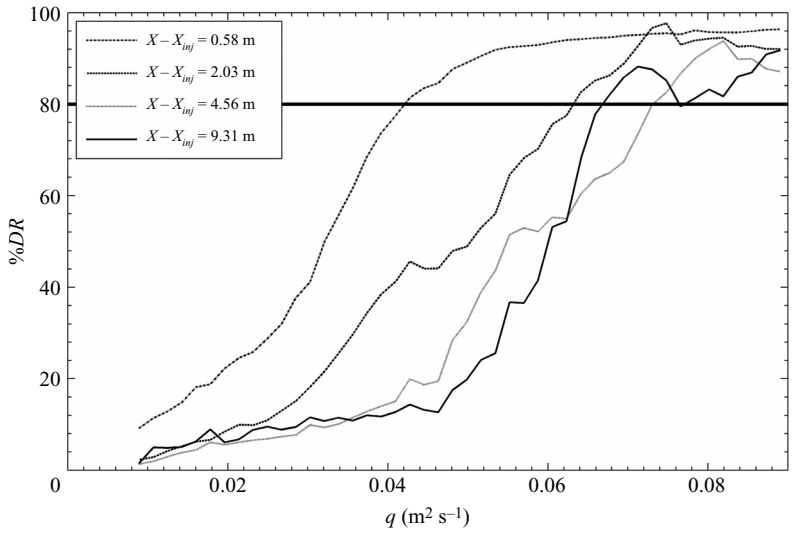

FIGURE 21. $\%DR$ versus q, the volumetric gas injection rate per unit span (m^2 s^{-1}) from Test 1b for 11.1 m s^{-1} at four downstream locations. The solid horizontal line at $\%DR = 80\,\%$ is the threshold used for defining ALDR.

To investigate further the transition from BDR to ALDR, we examine more carefully another location, $X - X_{inj} = 6.05$ m, not shown in figure 21. Three distinct regimes are apparent and identified in figure 22 with $\%DR$ versus q for 11.1 m s^{-1}: Region I, BDR zone where $\%DR$ increases linearly with gas injection rate; Region II, a transition zone between BDR and ALDR where the $\%DR$ versus q slope increases

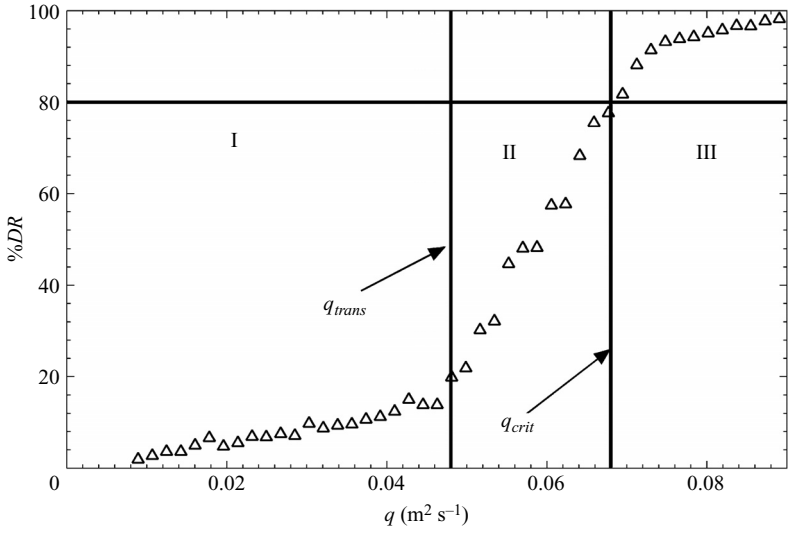

FIGURE 22. $\%DR$ versus q (m^2 s^{-1}) from Test 1b 11.1 m s^{-1} at $X - X_{inj} = 6.05$ m, which illustrates the three regimes of BDR and ALDR: I, a BDR regime where drag reduction is nearly linear with gas injection; II, a transitional region with a much steeper slope; and III, an ALDR regime where a maximum level of drag reduction is achieved.

dramatically relative to region I, but still exhibits linear change; and Region III, ALDR zone where the level of drag reduction has reached a maximum ($\sim$100 %) and increasing the gas injection rate shows little or no improvement in drag reduction owing to the near complete elimination of friction drag. Two gas injection-rate thresholds are defined; a transition threshold, q_{trans}, and a critical gas injection rate for ALDR, q_{crit}. These gas injection rates are located at the break point (abrupt slope change) between regions I and II (q_{trans}) and between regions II and III (q_{crit}) as seen in figure 22. Shown in figure 23 are the results for q_{crit} and q_{trans} from the primary experiment without surfactant in the background that define the transition between drag-reduction regimes.

3.3.2. *Scaling of air-layer drag reduction*

The gas injection-rate thresholds are observed to be influenced strongly by the free-stream velocity, as observed in figure 23 for the porous-plate injector without surfactant. The critical gas injection rates per unit span with and without surfactant in the tunnel background are shown in figure 24 as a function of free-stream velocity, U_∞. The lines shown in figure 24 are least mean-squares-error quadratic fits to the experimental data. The gas requirement for ALDR is about 5 to 10 % higher with surfactant in the tunnel background. This implies that the interfacial tension plays a role in the formation and/or the stability of the air layer. Though we do not fully understand this, we conjecture that the reduced surface tension (with surfactant present) allows the liquid–gas interface to deform more readily (decreased pressure with the same curvature); hence the liquid–gas interface allows larger fluctuations to occur, and a larger flux of gas is required to maintain the air layer. In addition, the small difference seen in figure 18 that shows less $\%DR$ with surfactant than without surfactant may manifest itself here.

Additionally, if a true air layer is formed between the model surface and the outer flow, the nominal thickness of the air layer, t_a, can be estimated using (3.2),

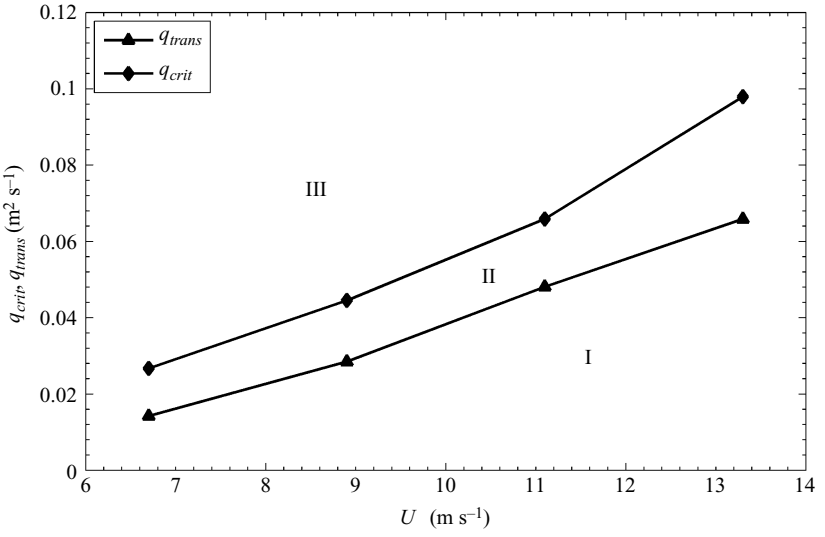

FIGURE 23. Transition gas injection rate, q_{trans} and critical gas injection rate, q_{crit}, ($m^2 s^{-1}$) versus free-stream speed determined from Test 1b data. These two curves define the boundaries for the three drag reduction regions: I, BDR; II, transition region between BDR and ALDR; and III, ALDR.

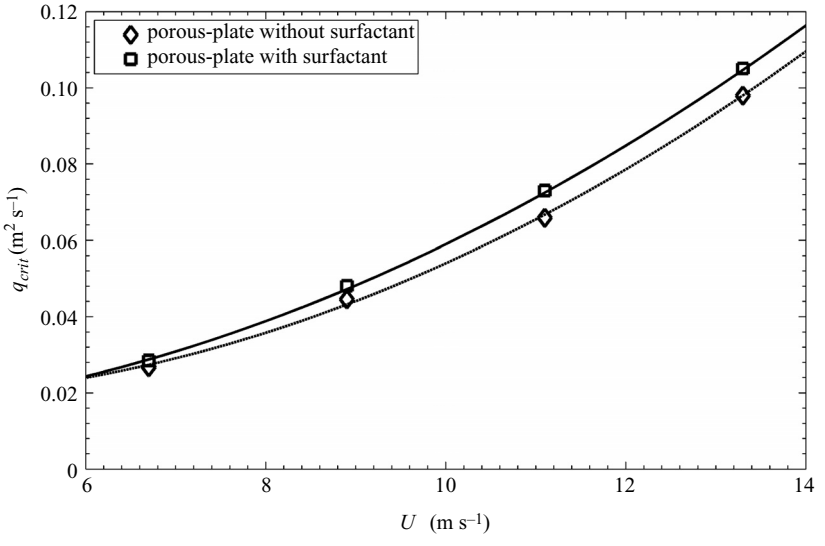

FIGURE 24. Critical gas injection rate, q_{crit} (m^2 s^{-1}), for ALDR for the porous-plate injector without (◇) and with surfactant (□) in the background tunnel volume. The lines represent a least-squares quadratic fit to the experimental data collected during Test 1b.

$t_a = Q_A/BU_\infty$, the same parameter as used successfully for the 'initial zone' scaling of BDR. Although no measurements of the velocity of the gas-phase were recorded, it is assumed presently that they are of the order of and proportional to the liquid free-stream velocity. Again, when the critical gas-injection rate is plotted with the corresponding nominal thickness, t_a, a linear relationship is observed as shown in

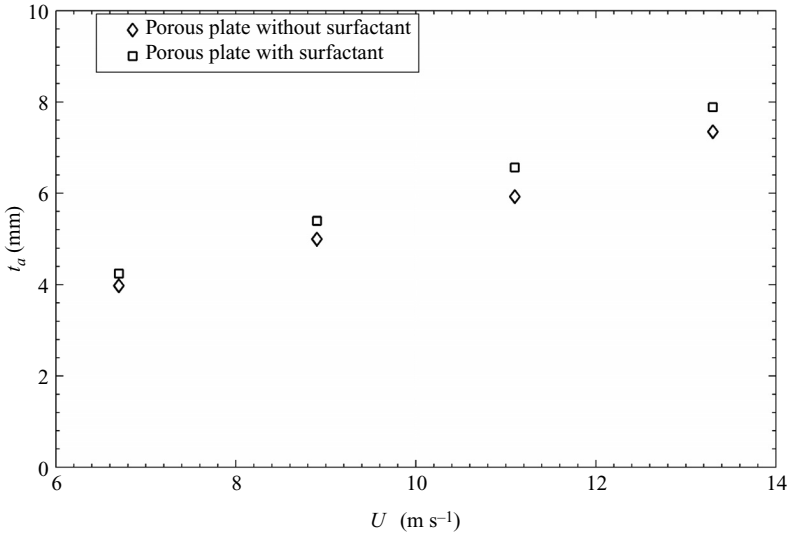

FIGURE 25. Critical air-layer thickness, $t_a = Q_A/BU_\infty$ as a function of free-stream speed, U_∞, for ALDR with injection from the porous-plate injector with and without surfactant in the tunnel background. These data were from Test 1b.

figure 25. And as can be seen in the figure, values of t_a from approximately 4 to 8 mm were required to maintain an air layer over the entire test model.

To provide perspective for our ALDR results, we resort to other large-scale experiments. The large-scale model tests on flat-bottom models, to 50 m in length, by the Japanese group at the National Maritime Research Institute (i.e. Kodama and co-workers) have exceeded the gas injection rates used here. However, a persistent air layer with dramatic drag reduction was not observed over the length of their models. At a speed of 7 m s^{-1}, with t_a about 4 mm, drag reduction exceeding 40 % was not observed beyond the first few metres of the 50 m test model of Kodama *et al.* (2002). The difference is possibly the result of spanwise gas diffusion on their test models. The test models used were at most 1 m in width, with gas injected over only the centre 50 %. Kodama *et al.* (2002) report that the spanwise uniformity of drag reduction was quite poor; it decreased linearly from the centreline to almost zero at the edge of the model. In addition, it is possible that gas could have escaped from beneath the test model as the models had no 'skegs' to help capture the air beneath the ship. Contrastingly, in the present experiments, gas was injected over nearly 90 % of the test model and it was 'trapped' beneath the model by the test-section sidewalls (i.e. the model spanned the entire width of the test section) perhaps explaining the difference in results.

3.3.3. *Roughness effects on ALDR*

The first supplementary experiment to help us to understand ALDR better involved a roughened model surface. As this configuration used a different injector design (Slot B rather than the porous plate), data were collected once again, as described above, initially on the smooth model for free-stream speeds ranging from 6.7 to 15.3 m s^{-1}. At the highest free-stream speed, 15.3 m s^{-1}, ALDR was observed on the skin-friction balances, but the required air flux exceeded the flow meter calibration range. At the conclusion of these additional smooth-surface experiments, the model

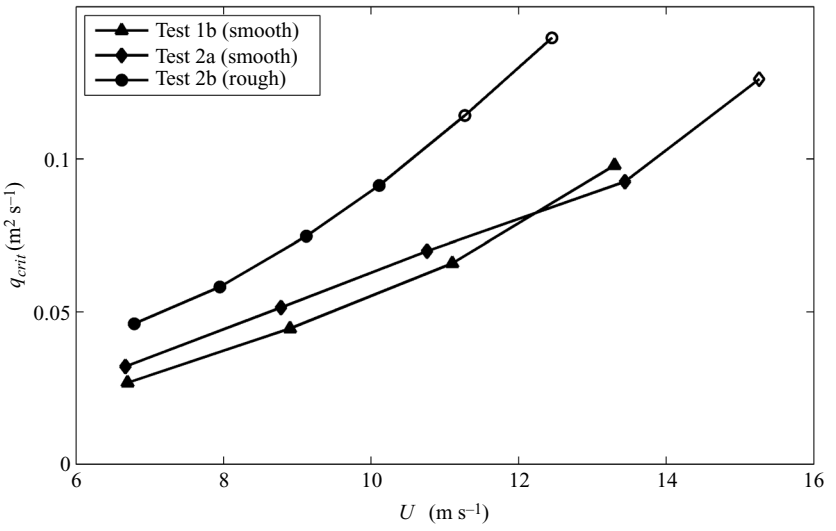

FIGURE 26. q_{crit} versus U_∞ for ALDR. Open symbols correspond to data points that exceeded the flow meter calibration range and are only estimates. Smooth-model ALDR experiments, Tests 1b and 2a were conducted about a year apart with different injector geometry. The roughened model, Test 2b, was tested immediately following Test 2a with the same injector.

was roughened and data were collected for free-stream speeds ranging from 6.8 to 12.5 m s^{-1}. Figure 26 shows q_{crit} for the two smooth-model tests and the rough-model experiment with outline data points corresponding to results that exceeded the calibration range of the flow meter. As is evident in the figure, while ALDR was observed for a given speed, it required about a 30 to 50 % larger volumetric gas flux to transition than did the smooth plate. Note further that the lower two curves in the figure exhibit reasonable repeatability – these first and second experiments with the hydraulically smooth plate were conducted about a year apart. In addition, the current results were scaled using the scaling proposed by Deutsch *et al.* (2003) for rough surfaces. However the scaling failed to collapse the data adequately, though the collapse was improved compared to the smooth-model results.

Video imaging of the flow captured BDR, the transition from BDR to ALDR, and ALDR. The imager was mounted outside the tunnel with a fixed view of the streamwise and spanwise directions of the test surface about 5 m downstream of the leading edge. Figure 27 shows still frames from the video at three instances during the injection process at a free-stream speed of 6.8 m s^{-1}. Figure 27(*a*) was recorded prior to air injection and shows the roughened model surface; figure 27(*b*) was recorded prior to achieving the critical volumetric flux to transition to ALDR (i.e. during BDR); and figure 27(*c*) was recorded following the transition to ALDR. In the no-injection frame (figure 27*a*) an instrumentation hatch (large outlined rectangle in lower right-hand corner) and a sampling port (dark, small rectangle in upper right used for a separate experiment) are clearly visible. As is typical of bubbly flows, even at low void fraction, the layer adjacent to the model surface becomes opaque during BDR (figure 27*b*) resulting in the disappearance of both the hatch and the sampling port. Once transitioned to ALDR (figure 27*c*), the layer becomes semi-transparent again as evidenced by the reappearance of the sampling port. These images support the concept that transition from BDR to ALDR corresponds to a change in flow regimes.

FIGURE 27. Images recorded during Test 2b of the roughened model surface at 6.8 m s^{-1}: (*a*) no injection; (*b*) bubble drag reduction; and (*c*) air-layer drag reduction. The streamwise (right to left in images) and spanwise (top to bottom in images) directions of the model were observed by the recording system.

3.3.4. *The importance of inflow conditions: use of a faired step*

In a third experiment to investigate air layers (as well as air cavities), we discovered that uniformity and lack of turbulent eddies with sizes greater than approximately 1 cm in the inflow TBL at the injection location were required to obtain ALDR with flush injection. This has important ramifications for implementation of ALDR. In the LCC, the unintentional disturbances were caused by an attempt at *in situ* repairs to the test-model surface upstream of the injector which resulted in a highly disturbed TBL upstream of the injector. After observing that we could no longer achieve ALDR at equivalent gas fluxes, a different injector configuration was implemented. This set-up included a 1 cm backward-facing step, faired upstream into the nose of the plate. Once installed, the step provided a clean separation line for the flow between the gas and the liquid. This allowed for the formation of air layers, although at increased air flux. This result indicates that care must be taken to ensure that the TBL upstream of an air-layer formation should be free of large-scale non-uniformities, and that the use of a small step can provide a clean flow separation for the air layer, even if the incoming TBL is not uniform.

4. Summary and conclusions

From the high-Reynolds-number drag-reduction experiments conducted on the test model, the following conclusions can be drawn with regard to bubble drag reduction (BDR). (i) Prior scaling laws developed by Madavan *et al.* (1984*a*), Deutsch *et al.* (2003), and Sanders *et al.* (2006) do not adequately collapse BDR and ALDR data for the range of parameters investigated. (ii) The present results near the point of injection ($X - X_{inj} = 0.6$ m) collapse using an 'initial zone' scaling and agree reasonably well with the results of Madavan *et al.* (iii) Drag reduction decays rapidly with downstream distance at higher free-stream speeds and drag reductions exceeding 10–20 % were not observed beyond about 2 m at 20.0 m s^{-1}. (iv) Injector geometry has only a marginal effect on the magnitude and persistence of drag reduction, at least for the two different geometries implemented. (v) Reducing the surface tension by employing a water-soluble surfactant has little effect on BDR away from the injector. (vi) Downstream of the injector, decreasing the surface tension has negligible effects on bubble size. (vii) Changes of TBL thickness by a factor of about two at the point of injection have little or no influence on BDR. (viii) Compound injection (gas injection through two injectors spaced in the streamwise direction) showed no improvement

over injecting the entire flux through a single injector, and under certain conditions compound injection reduced drag reduction by preventing the transition to ALDR.

The following conclusions arise from the air-layer drag reduction (ALDR) experiments conducted on the test model. (i) Drag reduction with injection of air can be divided into three distinct regions: Region I, a BDR zone, where drag reduction grows linearly with gas injection rate; Region II, a 'transition zone' where drag reduction increases linearly with a much steeper slope than in Region I; and Region III, an ALDR zone characterized by a thin air film between the test-model surface and the liquid free stream where 90 % $\pm$ 10 % drag reduction is observed and hence increasing injection rate yields little or no improvement in drag reduction. (ii) The 'critical' gas injection rate required to form a persistent air layer is approximately proportional to the square of the free-stream liquid velocity (or linearly proportional to the nominal air-layer thickness, $t_a = Q_a/BU_\infty$). (iii) The 'critical' gas injection rate was observed to increase slightly with surfactant solution in the tunnel volume. A drop in surface tension from 70 to $\sim$50 dyn cm^{-1}, increases the gas requirements by $\sim$10 %, implying that surface tension plays a role in the formation and stability of an air layer. (iv) ALDR was observed to persist over the entire length of model ($X - X_{inj} \sim 10$ m) at speeds to 15.3 m s^{-1} with no decay in the level of drag reduction. Therefore, it is conjectured that ALDR may have persistence lengths much greater than the length of the current test model. (v) Significantly increasing the surface roughness results in an increase in the critical volumetric flux for transition to ALDR, but a stable air layer still forms and was observed to free-stream speeds of 12.5 m s^{-1}. (vi) Inflow conditions can significantly affect the stability and formation of an air layer, but such sensitivity can be mitigated through the use of clean separation lines *via* a faired step.

The authors would like to thank the technical staff of the US Navy's William B. Morgan Large Cavitation Channel, especially Dr J. Michael Cutbirth and Mr Robert Etter. Mr Kent Pruss, Mr William Kirkpatrick and co-workers of the UM machine shops contributed substantially to the construction of the test model and instrumentation. Mr Duncan Brown of the Johns Hopkins University Applied Physics Laboratory and Dr Howard Petrie of the Pennsylvania State University provided helpful insight and advice. Others who have contributed to this research include Dr Wendy Sanders, Dr Shiyao Bian, Dr Xiaochun Shen, Dr Chinar Aphale, Dr Natasha Chang, and Ms Ciara Stella. This research was sponsored by DARPA under Contracts HR0011-04-1-001 and HR0011-06-1-0057 (Dr Thomas Beutner, Program Manager) and by ONR under Contract N00014-06-1-0244 (Dr L. Patrick Purtell, Program Manager). The content of this document does not necessarily reflect the position or the policy of the United States Government, and no official endorsement should be inferred.

REFERENCES

Bodgevich, V. G. & Evseev, A. R. 1976 The distribution of skin friction in a turbulent boundary layer of water beyond the location of gas injection. *Investigations of Boundary Layer Control* (in Russian), vol. 62. Thermophysics Institute Publishing House.

van den Berg, T. H., Luther, S., Lathrop, D. P. & Lohse, D. 2005 Drag reduction in bubbly Taylor–Couette turbulence. *Phys. Rev. Lett.* **94**, 044501.

Ceccio, S. L. & George, D. L. 1996 A review of electrical impedance techniques for the Trans. ASME I: measurement of multiphase flows. *Trans. ASME*: I *J. Fluids Engng* **118**, 391–399.

Cho, J., Perlin, M. & Ceccio, S. L. 2005 Measurement of near-wall stratified bubbly flows using electrical impedance. *Meas. Sci. Technol.* **16**, 1021–1029.

Clark, H. & Deutsch, S. 1991 Microbubble skin friction reduction on an axisymmetric body under the influence of applied axial pressure gradients. *Phys. Fluids* A **3**, 2948–2954.

Deutsch, S., Money, M., Fontaine, A. & Petrie, H. 2003 Microbubble drag reduction in rough walled turbulent boundary layers. *Proc. ASME–Fluids Engng Div. Summer Meeting* 2003, pp. 1–9.

Druzhinin, O. A. & Elghobashi, S. 1998 Direct numerical simulations of bubble-laden turbulent flows using two-fluid formulation. *Phys. Fluids* **10**, 685–697.

Etter R. J., Cutbirth, J. M., Ceccio, S. L., Dowling, D. R. & Perlin, M. 2005 High Reynolds number experimentation in the US Navy's William B. Morgan large cavitation channel. *Meas. Sci. Technol.* **16**(9), 1701–1709.

Fontaine, A. A. & Deutsch, S. 1992 The influence of the type of gas on the reduction of skin friction drag by microbubble injection. *Exps. Fluids* **13**, 128–136.

George, D. L., Iyer, C. O. & Ceccio, S. L. 2000 Measurement of the bubbly flow beneath partial attached cavities using electrical impedance probes. *Trans. ASME* I: *J. Fluids Engng* **122**, 2000.

Hewitt, G. F. 1978 *Measurement of Two-Phase Flow Parameters.* Academic.

Kawakita, C. & Takano, S. 2000 Microbubble skin friction reduction under the influence of pressure gradients and curved surfaces. *J. Soc. Naval Arch. Japan* **188**, 11–21.

Kawamura, T., Moriguchi, Y., Kato, H., Kakugawa, A. & Kodama, Y. 2003 Effect of bubble size on the microbubble drag reduction of a turbulent boundary layer. *Proc. ASME Fluids Engng Conf. Summer Meeting* 2003, pp. 1–8.

Kodama, Y., Kakugawa, A. & Takahashi, T. 1999 Preliminary experiments on microbubbles for drag reduction using a long flat plate ship. *ONR Workshop on Gas Based Surface Ship Drag Reduction* (Newport, USA), pp. 1–4.

Kodama, Y., Kakugawa, A., Takahashi, T. & Kawashima, H. 2000 Experimental study on microbubbles and their applicability to ships for skin friction reduction. *Intl J. Heat Fluid Flow* **21**, 582–588.

Kodama, Y., Kakugawa, A., Takahashi, T., Nagaya, S. & Sugiyama, K. 2002 Microbubbles: drag reduction mechanism and applicability to ships. *24th Symp. Naval Hydrodyn.* pp. 1–19.

Kodama, Y., Hori, T., Kawashima, M. M. & Hinatsu, M. 2006 A full scale microbubble experiment using a cement carrier. *Eur. Drag Reduction and Flow Control Meeting, Ischia, Italy*, pp. 1–2.

Lapham, G. S., Dowling, D. R. & Schultz, W. W. 1999 In situ force-balance tensiometry. *Exps. Fluids* **27**, 157–166.

Lapham, G. S., Dowling, D. R. & Schultz, W. W. 2001 Linear and nonlinear gravity–capillary water waves with a soluble surfactant. *Exps. Fluids* **30**, 448–457.

Lu, J., Fernández, A. & Tryggvason, G. 2005 The effect of bubbles on the wall drag of a turbulent channel flow. *Phys. Fluids* **17**, 095102.

Lumley, J. L. 1973 Drag reduction in turbulent flow by polymer additives. *J Polymer Sci. Macromol. Rev.* **7**, 283–290.

Lumley, J. L. 1977 Drag reduction in two phase and polymer flows. *Phys. Fluids* **20**, S64–S70.

McCormick, M. E. & Battacharyya, R. 1973 Drag reduction of a submersible hull by electrolysis. *Naval Engrs J.* **85**, 11–16.

Madavan, N. K., Deutsch, S. & Merkle, C. L. 1984*a* Reduction of turbulent skin friction by microbubbles. *Phys. Fluids* **27**, 356–363.

Madavan, N. K., Deutsch, S. & Merkle, C. L. 1984*b* Numerical investigation into the mechanisms of microbubble drag reduction. *Trans. ASME* I: *J. Fluids Engng* **107**, 370–377.

Madavan, N. K., Deutsch, S. & Merkle, C. L. 1985 Measurements of local skin friction in a microbubble modified turbulent boundary layer. *J. Fluid Mech.* **156**, 237–256.

Maxwell, J. 1881 *A Treatise on Electricity and Magnetism.* Clarendon.

Meng, J. C. S. & Uhlman, J. S. 1989 Microbubble formulation and splitting in a turbulent boundary layer for turbulence reduction. *Advances in Fluid Dynamics*, pp. 168–217. Springer.

Meng, J. C. S. & Uhlman, J. S. 1998 Microbubble formation and splitting in a turbulent boundary layer for turbulence reduction. *Proc. Intl Symp. Seawater Drag Reduction*, pp. 341–355.

Merkle, C. & Deutsch, S. 1990 Drag reduction in liquid boundary layers by gas injection. *Viscous Drag Reduction in Boundary Layers* (ed. D. M. Bushnel & J. N. Hefner). *Progress in Astronautics and Aeronautics AIAA* **123**, 351–412.

Merkle, C. & Deutsch, S. 1992 Microbubble drag reduction in liquid turbulent boundary layers. *Appl. Mech. Rev.* **45**, 103–127.

Nagamatsu, T., Kodama, T., Kakugawa, A., Takai, M., Murakami, K., Ishikawa., Kamiirisa, H., Ogiwara, S., Yoshida, Y., Suzuki, T., Toda, Y., Kato, H., Ikemoto, A., Yamatani, S., Imo, S. & Yamashita, K. 2002 A full-scale experiment on microbubbles for skin friction reduction using SEIUN MARU. Part 2: The full-scale experiment. *J. Soc. Naval Arch. Japan* **192**, 15–28.

Nagaya, S., Kakugawa, A., Kodama, Y. & Hishida, K. 2001 PIV/LIF measurements on 2-D turbulent channel flow with microbubbles. *4th Intl Symp. on PIV, Goettingen, Germany*.

Oweis, G. F., Winkel, E. S., Cutbirth, J. M., Perlin, M., Ceccio, S. L. & Dowling, D. R. 2008 Smooth-flat-plate turbulent boundary layer measurements at high Reynolds number. *J. Fluid Mech.* (submitted).

Pal, S., Deutsch, S. & Merkle, C. L. 1989 A comparison of shear stress fluctuation statistics between microbubble modified and polymer modified turbulent flow. *Phys. Fluids* A **1**, 1360–1362.

Sanders, W. C. 2004 Bubble drag reduction in a flat plate boundary layer at high Reynolds numbers and large scales. Doctoral thesis, University of Michigan.

Sanders, W. C., Winkel, E. S., Dowling, D. R., Perlin, M. & Ceccio, S. L. 2006 Bubble friction drag reduction in a high-Reynolds-number flat-plate turbulent boundary layer. *J. Fluid Mech.* **552**, 353–380.

Schultz-Grunow, F. 1941 New frictional resistance law for smooth plates. *NACA TM* **17**, 1–24

Shen, X., Perlin, M. & Ceccio, S. L. 2006 Influence of bubble size on micro-bubble drag reduction. *Exps. Fluids* **41**, 415–424.

Takahashi, T., Kakugawa, A., Nagaya, S., Yanagihara, T. & Kodama, Y. 2001 Mechanisms and scale effects of skin friction reduction by microbubbles. *Proc. 2nd Symp. on the Smart Control of Turbulence, University of Tokyo*, pp. 1–9.

Watanabe, O., Masuko, A. & Shirose, Y. 1998 Measurements of drag reduction by microbubbles using very long ship models. *J. Soc. Naval Arch. Japan* **183**, 53–63.

White, F. M. 1991 *Viscous Fluid Flow*. McGraw-Hill.

Winkel, E. S. 2007 High Reynolds number flat plate turbulent boundary layer measurements and skin friction drag reduction with gas or polymer injection. Doctoral thesis, University of Michigan.

Winkel, E. S., Ceccio, S. L., Dowling, D. R. & Perlin, M. 2004 Bubble size distributions produced by wall-injection of air into flowing freshwater, saltwater, and surfactant solutions. *Exps. Fluids* **37**, 802–810.